

**Precision Measurements
of the Neutral Current
from Hadron and Lepton Production at LEP**

The OPAL Collaboration

Abstract

New measurements of the hadronic and leptonic cross sections and of the leptonic forward-backward asymmetries in e^+e^- collisions are presented. The analysis includes data recorded up to the end of 1991 by the OPAL experiment at LEP, with centre-of-mass energies within ± 3 GeV of the Z^0 mass. The results are based on a recorded total of 454 000 hadronic and 58 000 leptonic events. A model independent analysis of Z^0 parameters based on an extension of the improved Born approximation is presented leading to tests of lepton universality and an interpretation of the results within the Standard Model framework. The determination of the mass and width of the Z^0 benefit from an improved understanding of the LEP energy calibration.

Submitted to Z. Phys. C

The OPAL Collaboration

P.D. Acton²⁵, G. Alexander²³, J. Allison¹⁶, P.P. Allport⁵, K.J. Anderson⁹, S. Arce², A. Astbury²⁸,
D. Axen²⁹, G. Azuelos^{18,a}, G.A. Bahan¹⁶, J.T.M. Baines¹⁶, A.H. Ball¹⁷, J. Banks¹⁶, R.J. Barlow¹⁶,
S. Barnett¹⁶, J.R. Batley⁵, G. Beaudoin¹⁸, A. Beck²³, G.A. Beck¹³, J. Becker¹⁰, T. Behnke²⁷,
K.W. Bell²⁰, G. Bella²³, P. Bentkowsky¹⁸, P. Berlich¹⁰, S. Bethke¹¹, O. Biebel³, U. Binder¹⁰,
I.J. Bloodworth¹, P. Bock¹¹, B. Boden³, H.M. Bosch¹¹, H. Breuer⁸, P. Bright-Thomas²⁵,
R.M. Brown²⁰, A. Buijs⁸, H.J. Burckhardt⁸, C. Burgard²⁷, P. Capiluppi², R.K. Carnegie⁶, A.A. Carter¹³,
J.R. Carter⁵, C.Y. Chang¹⁷, D.G. Charlton⁸, S.L. Chu⁴, P.E.L. Clarke²⁵, I. Cohen²³, J.C. Clayton¹,
W.J. Collins⁵, J.E. Conboy¹⁵, M. Cooper²², M. Coupland¹⁴, M. Cuffiani², S. Dado²², G.M. Dallavalle²,
S. De Jong¹³, L.A. del Pozo⁵, H. Deng¹⁷, A. Dieckmann¹¹, M. Dittmar⁴, M.S. Dixit⁷, E. do Couto e
Silva¹², J.E. Duboscq⁸, E. Duchovni²⁶, G. Duckeck¹¹, I.P. Duerdoth¹⁶, D.J.P. Dumas⁶, P.A. Elcombe⁵,
P.G. Estabrooks⁶, E. Etzion²³, H.G. Evans⁹, F. Fabbri², M. Fierro², M. Fincke-Keeler²⁸, H.M. Fischer³,
D.G. Fong¹⁷, M. Foucher¹⁷, A. Gaidot²¹, O. Ganel²⁶, J.W. Gary⁴, J. Gascon¹⁸, R.F. McGowan¹⁶,
N.I. Geddes²⁰, C. Geich-Gimbel³, S.W. Gensler⁹, F.X. Gentit²¹, G. Giacomelli², R. Giacomelli²,
V. Gibson⁵, W.R. Gibson¹³, J.D. Gillies²⁰, J. Goldberg²², M.J. Goodrick⁵, W. Gorn⁴, C. Grandi²,
F.C. Grant⁵, J. Hagemann²⁷, G.G. Hanson¹², M. Hansroul⁸, C.K. Hargrove⁷, P.F. Harrison¹³, J. Hart⁸,
P.M. Hattersley¹, M. Hauschild⁸, C.M. Hawkes⁸, E. Heflin⁴, R.J. Hemingway⁶, R.D. Heuer⁸, J.C. Hill⁵,
S.J. Hillier⁸, T. Hilde¹⁰, D.A. Hinshaw¹⁸, J.D. Hobbs⁸, P.R. Hobson²⁵, D. Hochman²⁶, R.J. Homer¹,
A.K. Honma^{28,a}, R.E. Hughes-Jones¹⁶, R. Humbert¹⁰, P. Igo-Kemenes¹¹, H. Ihssen¹¹, D.C. Imrie²⁵,
A.C. Janissen⁶, A. Jawahery¹⁷, P.W. Jeffreys²⁰, H. Jeremie¹⁸, M. Jimack², M. Jobes¹, R.W.L. Jones¹³,
P. Jovanovic¹, C. Jui⁴, D. Karlen⁶, K. Kawagoe²⁴, T. Kawamoto²⁴, R.K. Keeler²⁸, R.G. Kellogg¹⁷,
B.W. Kennedy¹⁵, S. Kluth⁵, T. Kobayashi²⁴, D.S. Koetke⁸, T.P. Kokott³, S. Komamiya²⁴, L. Köpke⁸,
J.F. Kral⁸, R. Kowalewski⁶, J. von Krogh¹¹, J. Kroll⁹, M. Kuwano²⁴, P. Kyberd¹³, G.D. Lafferty¹⁶,
R. Lahmann¹⁷, F. Lamarche¹⁸, J.G. Layter⁴, P. Leblanc¹⁸, A.M. Lee¹⁷, M.H. Lehto¹⁵, D. Lellouch²⁶,
C. Leroy¹⁸, J. Letts⁴, S. Levegrün³, L. Levinson²⁶, S.L. Lloyd¹³, F.K. Loebinger¹⁶, J.M. Lorah¹⁷,
B. Lorazo¹⁸, M.J. Losty⁷, X.C. Lou¹², J. Ludwig¹⁰, M. Mannelli⁸, S. Marcellini², G. Maringer³,
C. Markus³, A.J. Martin¹³, J.P. Martin¹⁸, T. Mashimo²⁴, P. Mättig³, U. Maur³, J. McKenna²⁸,
T.J. McMahon¹, J.R. McNutt²⁵, F. Meijers⁸, D. Menszner¹¹, F.S. Merritt⁹, H. Mes⁷, A. Michelini⁸,
R.P. Middleton²⁰, G. Mikenberg²⁶, J. Mildener⁶, D.J. Miller¹⁵, R. Mir¹², W. Mohr¹⁰, C. Moisan¹⁸,
A. Montanari², T. Mori²⁴, M. Morii²⁴, T. Mouthuy^{12,b}, B. Nellen³, H.H. Nguyen⁹, M. Nozaki²⁴,
S.W. O'Neale¹, F.G. Oakham⁷, F. Odorici², H.O. Ogren¹², C.J. Oram^{28,a}, M.J. Oreglia⁹, S. Orito²⁴,
J.P. Pansart²¹, B. Panzer-Steindel⁸, P. Paschivici²⁶, G.N. Patrick²⁰, N. Paz-Jaoshvili²³, P. Pfister¹⁰,
J.E. Pilcher⁹, J. Pinfold³¹, D. Pitman²⁸, D.E. Plane⁸, P. Poffenberger²⁸, B. Poli², A. Pouladdej⁶,
T.W. Pritchard¹³, H. Przysiezniak¹⁸, G. Quast²⁷, M.W. Redmond⁹, D.L. Rees⁸, G.E. Richards¹⁶,
D. Robinson⁸, A. Rollnik³, J.M. Roney^{28,c}, E. Ros⁸, S. Rossberg¹⁰, A.M. Rossi², M. Rosvick²⁸,
P. Routenburg⁶, K. Runge¹⁰, O. Runolfsson⁸, D.R. Rust¹², M. Sasaki²⁴, C. Sbarra⁸, A.D. Schaile¹⁰,
O. Schaile¹⁰, W. Schappert⁶, P. Scharff-Hansen⁸, P. Schenk⁴, B. Schmitt³, H. von der Schmitt¹¹,
S. Schreiber³, C. Schwick²⁷, J. Schwiening³, W.G. Scott²⁰, M. Settles¹², T.G. Shears⁵, B.C. Shen⁴,
C.H. Shepherd-Themistocleous⁷, P. Sherwood¹⁵, R. Shypit²⁹, A. Simon³, P. Singh¹³, G.P. Sirotti²,
A. Skuja¹⁷, A.M. Smith⁸, T.J. Smith²⁸, G.A. Snow¹⁷, R. Sobie^{28,c}, R.W. Springer¹⁷, M. Sproston²⁰,
K. Stephens¹⁶, J. Steuerer²⁸, R. Ströhmer¹¹, D. Strom³⁰, T. Takeshita^{24,d}, P. Taras¹⁸, S. Tarem²⁶,
M. Tecchio⁹, P. Teixeira-Dias¹¹, N. Tesch³, N.J. Thackray¹, M.A. Thomson¹⁵, E. Torrente-Lujan²²,
G. Transtromer²⁵, N.J. Tresilian¹⁶, T. Tsukamoto²⁴, M.F. Turner⁸, G. Tysarczyk-Niemeyer¹¹, D. Van
den plas¹⁸, R. Van Kooten²⁷, G.J. VanDalen⁴, G. Vasseur²¹, C.J. Virtue⁷, A. Wagner²⁷, D.L. Wagner⁹,
C. Wahl¹⁰, J.P. Walker¹, C.P. Ward⁵, D.R. Ward⁵, P.M. Watkins¹, A.T. Watson¹, N.K. Watson⁸,
M. Weber¹¹, P. Weber⁶, P.S. Wells⁸, N. Wermes³, M.A. Whalley¹, G.W. Wilson⁴, J.A. Wilson¹,
V.-H. Winterer¹⁰, T. Wlodek²⁶, S. Wotton¹¹, T.R. Wyatt¹⁶, R. Yaari²⁶, A. Yeaman¹³, G. Yekutieli²⁶,
M. Yurko¹⁸, W. Zeuner⁸, G.T. Zorn¹⁷.

- ¹School of Physics and Space Research, University of Birmingham, Birmingham, B15 2TT, UK
- ²Dipartimento di Fisica dell' Università di Bologna and INFN, Bologna, 40126, Italy
- ³Physikalisches Institut, Universität Bonn, D-5300 Bonn 1, FRG
- ⁴Department of Physics, University of California, Riverside, CA 92521 USA
- ⁵Cavendish Laboratory, Cambridge, CB3 0HE, UK
- ⁶Carleton University, Dept of Physics, Colonel By Drive, Ottawa, Ontario K1S 5B6, Canada
- ⁷Centre for Research in Particle Physics, Carleton University, Ottawa, Ontario K1S 5B6, Canada
- ⁸CERN, European Organisation for Particle Physics, 1211 Geneva 23, Switzerland
- ⁹Enrico Fermi Institute and Department of Physics, University of Chicago, Chicago Illinois 60637, USA
- ¹⁰Fakultät für Physik, Albert Ludwigs Universität, D-7800 Freiburg, FRG
- ¹¹Physikalisches Institut, Universität Heidelberg, Heidelberg, FRG
- ¹²Indiana University, Dept of Physics, Swain Hall West 117, Bloomington, Indiana 47405, USA
- ¹³Queen Mary and Westfield College, University of London, London, E1 4NS, UK
- ¹⁴Birkbeck College, London, WC1E 7HV, UK
- ¹⁵University College London, London, WC1E 6BT, UK
- ¹⁶Department of Physics, Schuster Laboratory, The University, Manchester, M13 9PL, UK
- ¹⁷Department of Physics, University of Maryland, College Park, Maryland 20742, USA
- ¹⁸Laboratoire de Physique Nucléaire, Université de Montréal, Montréal, Quebec, H3C 3J7, Canada
- ²⁰Rutherford Appleton Laboratory, Chilton, Didcot, Oxfordshire, OX11 0QX, UK
- ²¹DAPNIA/SPP, Saclay, F-91191 Gif-sur-Yvette, France
- ²²Department of Physics, Technion-Israel Institute of Technology, Haifa 32000, Israel
- ²³Department of Physics and Astronomy, Tel Aviv University, Tel Aviv 69978, Israel
- ²⁴International Centre for Elementary Particle Physics and Dept of Physics, University of Tokyo, Tokyo 113, and Kobe University, Kobe 657, Japan
- ²⁵Brunel University, Uxbridge, Middlesex, UB8 3PH UK
- ²⁶Nuclear Physics Department, Weizmann Institute of Science, Rehovot, 76100, Israel
- ²⁷Universität Hamburg/DESY, II Inst für Experimental Physik, 2000 Hamburg 52, Germany
- ²⁸University of Victoria, Dept of Physics, P O Box 3055, Victoria BC V8W 3P6, Canada
- ²⁹University of British Columbia, Dept of Physics, 6224 Agriculture Road, Vancouver BC V6T 1Z1, Canada
- ³⁰University of Oregon, Dept of Physics, Eugene, Oregon 97403, USA
- ³¹University of Alberta, Dept of Physics, Edmonton AB T6G 2J1, Canada

^aAlso at TRIUMF, Vancouver, Canada V6T 2A3

^bNow at Centre de Physique des Particules de Marseille, Faculté des Sciences de Luminy, Marseille

^cAnd IPP, University of Victoria, Dept of Physics, P O Box 3055, Victoria BC V8W 3P6, Canada

^dAlso at Shinshu University, Matsumoto 390, Japan

1 Introduction

We present hadronic and leptonic cross sections and leptonic forward-backward asymmetries measured in e^+e^- collisions at centre-of-mass energies, \sqrt{s} , within ± 3 GeV of the Z^0 mass, M_Z . The data were recorded during 1991 by the OPAL experiment at LEP. These are combined with our published cross sections and asymmetries, from data available at the end of 1990 [1], in order to improve the determination of electroweak parameters and provide a more stringent test of the Standard Model.

The integrated luminosity of the 1991 dataset is approximately 14 pb^{-1} , more than double that of the 1990 data [1]. The first 40% of the 1991 luminosity was accumulated at a fixed centre-of-mass energy at approximately the Z^0 mass. The remainder was recorded during scans of seven energy points around the Z^0 mass.

The larger 1991 data sample has allowed more detailed systematic studies to be made, leading to a reduction of the systematic errors for all analyses presented. The luminosity measurement has benefited from an additional set of forward drift chambers, installed in 1992, which provides a more precise survey of the acceptance for luminosity events. The selection of hadronic events has been improved by extending the acceptance to regions closer to the beam pipe.

This analysis also makes use of a recent improvement in the energy calibration of the LEP beams [2], which has resulted in a considerable reduction of the systematic uncertainty on the Z^0 mass and total width, Γ_Z , as well as a shift in the measured value of M_Z with respect to our previously published value.

A description of the OPAL detector and Monte Carlo programs is given in section 2. The luminosity measurement and the hadronic and leptonic event selections are described in sections 3, 4 and 5, respectively. The results of the LEP energy calibration are given in section 6 and the determination of electroweak parameters is presented in section 7. Finally, the results are summarized in section 8.

2 The OPAL Detector and Simulation

The OPAL detector is described in detail elsewhere [3]. The trajectories of charged particles are measured using a precision vertex drift chamber, a jet chamber and z-chambers, inside a solenoidal coil. This is surrounded by a time-of-flight counter array and a lead glass electromagnetic calorimeter with a presampler, which measures the positions and energies of showering particles. Outside this are a hadron calorimeter and four layers of muon chambers. Forward detectors are used for measuring the luminosity. A right-handed coordinate system is adopted by OPAL, where the x axis points to the centre of the LEP ring, and positive z is along the electron beam direction. The angles θ and ϕ are the polar and azimuthal angles, respectively.

For the generation of Monte Carlo $e^+e^- \rightarrow$ hadrons events we used the JETSET [4] and HERWIG [5] programs with parameter sets optimized by a study of global event shape variables in OPAL data [6]. The KORALZ [7] program was used for $e^+e^- \rightarrow \mu^+\mu^-$ and $e^+e^- \rightarrow \tau^+\tau^-$, and BABAMC [8] and BHLUMI [9] for the process $e^+e^- \rightarrow e^+e^-$. The detector response was simulated by a program [10] that treated in detail the detector geometry and material as well as the effects of detector resolution and efficiency. The simulated events were then reconstructed by the same procedure that was used to analyse the OPAL data.

3 The Luminosity Measurement

The integrated luminosity of the colliding beams at OPAL was determined from the number of small-angle Bhabha scattering events observed in two identical forward detectors located at either side of the interaction region. The forward detector is described in detail in [3, 11] and is shown schematically in Figure 1. The method used to determine the luminosity was similar to that employed for the 1990 data [1] and uses information from three elements of each forward detector. A lead-scintillator calorimeter measures the energy and position of small-angle electromagnetic showers. Three layers of proportional tube chambers are situated after the four radiation lengths of the presampler section of each calorimeter. The coordinates reconstructed from these tube chambers have a spatial resolution of about 3.5 mm, considerably better than those obtained from the calorimeter. For this reason tube coordinates were used to select events within a well defined acceptance. Calorimeter coordinates were used only if tube chamber information was unavailable or ambiguous. In order to reject spurious clusters only the largest energy calorimeter cluster at each end was considered and the tube clusters nearest to it in ϕ . In front of each calorimeter there are two planes of drift chambers. The drift chambers are the most precisely located element in the forward detector and are used to determine the positions of the tube chambers.

There has been one major improvement in the analysis presented here compared to that described in our previous publication [1]. For 1992 an additional set of drift chambers has been installed in front of the existing drift chambers. The sense wires of these chambers are located close to the inner edge of the acceptance used to select Bhabha events for the luminosity analysis. By using the data from these new chambers it was possible to survey the locations of the tube chambers in 1992 with a greatly reduced systematic uncertainty. It was demonstrated that the positions and performance of the tube chambers did not change between 1991 and 1992, and it was therefore possible to apply retrospectively the improved 1992 drift chamber survey of the tube positions to the 1991 data.

In order to eliminate any first-order dependence of the Bhabha acceptance on the relative positions of the forward detectors with respect to the e^+e^- interaction point, the acceptance was defined in terms of the average of the angles determined at the two sides, $\bar{\theta} = (\theta_R + \theta_L)/2$, and $\bar{\phi} = (\phi_R + \phi_L - 180^\circ)/2$, where (θ_L, ϕ_L) and (θ_R, ϕ_R) are the polar and azimuthal angles of the forward detector clusters to the left and right of the interaction region. The following criteria were used to define Bhabha events for the absolute luminosity determination:

- $65 \text{ mrad} < \bar{\theta} < 105 \text{ mrad}$;
- $55 \text{ mrad} < \theta_{L,R} < 115 \text{ mrad}$;
- $\bar{\phi} > 15^\circ$ away from vertical and horizontal axes;
- Acoplanarity $|\Delta\phi - 180^\circ| < 20^\circ$, where $\Delta\phi = |\phi_R - \phi_L|$;
- $E_L + E_R > (2/3)\sqrt{s}$;
- $E_{L,R} > 0.225\sqrt{s}$.

Here E_L, E_R are the energies deposited in the left and right forward detectors. These cuts are more restrictive than those used in [1].

Using the redundancy in the forward detector trigger [12], the trigger inefficiency for the above event selections was determined to be less than 0.02%. The background from random coincidences

was estimated to be less than 0.01% by counting coincidences between high energy clusters at opposite sides of the interaction point in pairs of events that were separated by the revolution period of the LEP beam. The contamination from $e^+e^- \rightarrow \gamma\gamma$ was calculated to be 0.16% [13]. Other backgrounds were shown to be negligible.

To investigate possible reconstruction problems all events with a well contained cluster with energy of greater than 40 GeV at one end but less than 10 GeV at the other end were studied in detail. Nearly all of these events were found to be consistent with initial state radiation leading to highly acollinear event topologies. From this study we determined the uncertainty of the luminosity measurement due to reconstruction inefficiencies to be $< 0.01\%$.

The effective Bhabha cross section for the luminosity measurement was calculated with events generated using the BHLUMI Monte Carlo [9] and a full simulation of the response of the forward detector [10]. The systematic uncertainty from the detector simulation was estimated to be 0.20% by varying the event selection cuts.

In BHLUMI the γ - Z^0 interference term is treated at the Born level only. It has recently been shown that this approximation is not sufficient at the required level of precision [14]. As a consequence of initial state radiation the interference term is no longer purely antisymmetric about $\sqrt{s} = M_Z$ and is significantly non-zero at $\sqrt{s} = M_Z$. The results of the BHLUMI [9] program have been compared with the results from the programs BABAMC [8] and BHAGEN [15]. In the latter two programs, the interference term is calculated including the effects of initial state radiation to first order in α . Once a common absolute normalization is imposed, the results of BABAMC and BHAGEN are in excellent agreement with each other for the energy dependence of the small angle Bhabha cross section, but both differ significantly from BHLUMI. In light of this, the program BABAMC was used for the calculation of the interference term. This results in a correction of 0.27% to the BHLUMI cross section at $\sqrt{s} = M_Z$ and a shift in the value of M_Z up by 1.2 MeV and Γ_Z down by 3.4 MeV. The corrected acceptance for the event selections described above was determined to be 12.713 nb at $\sqrt{s}=91.1$ GeV (including the contribution from $e^+e^- \rightarrow \gamma\gamma$). The theoretical uncertainty on the accepted Bhabha cross section from BHLUMI is 0.25% [9]. To account for the uncertainty in the interference term a total theoretical uncertainty of 0.30% [16] is assumed.

The precision of the luminosity determination depends on how well the geometrical acceptance can be defined. The distance along the beam axis between the two forward detectors was measured with a precision of ± 1 mm, resulting in a 0.04% uncertainty in luminosity. One of the dominant contributions to the systematic error on the absolute luminosity arises from the uncertainty in the radial positions (relative to the beam axis) of clusters reconstructed in the tube chambers. The absolute radial positions of the tube chambers are not *a priori* known with the precision required for the luminosity determination. Even if the physical locations of the tubes were known, systematic biases could result from many sources, for example from dead or inefficient tubes, or from variations in gain. The forward detector drift chambers, whose positions are precisely known, were used to determine the location of the tube chambers by comparing the position of clean electron tracks in the drift chambers with the reconstructed cluster position from the tube chambers.

In the analysis of the 1990 data [1] the then existing drift chambers were used to survey the positions of tubes in the region of the drift chamber sense wires (at approximately 100 mrad). The important inner edge cut was made at 58 mrad. The uncertainty on the precise pitch of the tube chambers led to a 0.4% systematic error on the luminosity arising from the extrapolation from the survey at 100 mrad to the inner edge cut at 58 mrad. In 1992 an additional set of drift chambers, the small angle reference chambers, was installed in front of the existing drift chambers. The sense wires of the chambers installed in 1992 are located at approximately 65 mrad, close to the inner edge

of the acceptance for the Bhabha events used in the 1991 luminosity determination. Data collected in 1992 were used to determine the locations of the tubes and this measurement has been used for the interpretation of the data recorded during 1991. This resulted in two distinct improvements in the analysis: the locations of the tubes were determined in the region of the inner edge cut and by using this additional drift chamber data it has been possible to improve greatly the systematic checks of the survey of the tube chamber positions. The uncertainty on the measurement arises from three separate sources: the uncertainty on the absolute positions of the drift chamber sense wires, the precision of the procedure used to determine the locations of the wires in terms of tube coordinates and the relative uncertainty between 1991 and 1992 in the location of clusters reconstructed with the tube chambers.

The separation of the drift chamber sense wires in diagonally opposite chambers at the same end was measured with a precision of $91 \mu\text{m}$. This uncertainty is completely correlated between all four such measurements. The z separation of the wires and tube chambers (parallel to the beam axis) is known with a precision of 0.5 mm for each forward detector. These two uncertainties in the locations of the drift chamber wires result in a 0.10% error in the luminosity.

The images of the drift chamber sense wires were located in the tube coordinate system by two methods of analysis, with largely independent systematic errors. The mean positions of the newly installed and existing drift chamber sense wires in tube chamber coordinates were determined with precisions of $98 \mu\text{m}$ and $118 \mu\text{m}$ respectively, resulting in a systematic error in the luminosity of 0.21% . This error estimate includes the statistical precision of the analysis and systematic contributions estimated from the differences in the results of the two methods, and from the effect of varying all the cuts in the analysis. The uncertainty in the absolute positions of the ϕ boundaries of the Bhabha acceptance, arising from the resulting $8 \mu\text{m}$ uncertainty in the mean pitch of the tube chambers (9.67 mm), led to a further 0.08% contribution to the error on the luminosity.

For the survey of the tube positions using 1992 data to be applicable to 1991 data it is necessary to demonstrate that the tube chambers could not physically move between the two years. The tube chambers are embedded in the forward detector calorimeter between the pre-sampler and main calorimeter. Each calorimeter is constructed in two halves which are brought together at the beginning of each year of data collection. The reproducibility with which the halves are brought together is ensured by dowel pins at the front and rear faces of the calorimeter. The fit at the dowels is estimated to be $\pm 20 \mu\text{m}$ and, allowing for any distortions, the separation of the tube chambers cannot vary by more than $100 \mu\text{m}$. It is also vital that the performance of the tube chambers was constant between the two years. Several tests were made of this assumption. Figure 2 shows one such demonstration of the consistency of the tube data between the two years. The precision of the tests led to the assignment of a 0.06% contribution to the systematic error on the luminosity for using the 1992 survey for the 1991 data.

Inhomogeneity in tube chamber reconstruction and evidence for a systematic shift in the drift chamber survey in one quadrant led to the assignment of an additional 0.30% contribution to the systematic uncertainty. One method used to quantify this effect was to examine the variation in luminosity as measured in different sectors of the acceptance. As in our previous publication [1] we divided the acceptance in ϕ into eight identical telescopes and calculated a luminosity in each one. The r.m.s. variation in the eight measurements was 0.9% . If it is assumed that each of the eight telescopes gives an independent measurement of the statistical and systematic error then the error in the overall luminosity is estimated to be less than 0.30% , once the statistical contribution is removed. The error estimate derived from this analysis was independent of the number of telescopes into which the acceptance was divided.

No significant bias was introduced by the 2.4% of clusters whose coordinates came from the

calorimeter alone; when the analysis was repeated using only calorimeter coordinates the luminosity changed by 1.6%. We estimate the systematic uncertainty resulting from the use of calorimeter coordinates to be 0.04%.

The contributions to the error on the absolute luminosity at the peak energy point are listed in Table 1. The individual contributions were added in quadrature to give an overall experimental error of 0.60%. Of this error 0.40% was due to finite data and Monte Carlo statistics. When the theoretical uncertainty of 0.30% is included the final error becomes 0.67%.

The relative luminosity measurement was essentially the same as that described in our previous publication [1]. The point-to-point relative luminosity error was dominated by small fill-to-fill fluctuations in the energy calibration of the forward detector calorimeter. This error scaled as $0.2\%/\sqrt{N_{\text{fills}}}$, where N_{fills} is the number of fills at each energy point. Since N_{fills} was always at least five, the systematic uncertainty in the relative luminosity was less than 0.1% at any one of the scan points and therefore negligible compared to the statistical uncertainty.

4 The Hadronic Decay Channel

In our previous publication [1], the criteria used to select hadronic Z^0 decays were based on energy clusters in the lead glass electromagnetic calorimeter and the charged track multiplicity. The accuracy of the acceptance calculation for this selection was limited by a 0.3% systematic uncertainty due to modelling of fragmentation. For the 1991 data, energy clusters in the forward detector calorimeter were also used in order to increase the geometrical acceptance and therefore reduce the sensitivity to the fragmentation model. Furthermore, invariant mass cuts were used to reduce background contamination, in particular from the process $e^+e^- \rightarrow \tau^+\tau^-$.

The following five requirements defined an hadronic candidate:

- The sum of the multiplicity of charged tracks and clusters in the lead glass was required to be at least 12.
- A high visible energy was required in the lead glass and the forward detector:

$$R_{vis} \equiv \left(\sum E_{clus} + \frac{1}{3} \sum E_{fdet} \right) / \sqrt{s} > 0.09,$$

where E_{clus} and E_{fdet} are the energies of each cluster in the lead glass and in the forward detector, respectively.

- The energy imbalance along the beam direction had to satisfy

$$R_{bal} \equiv \left| \sum (E_{clus} \cos \theta) + \sum (E_{fdet} \cos \theta) \right| / \left(\sum E_{clus} + \sum E_{fdet} \right) < 0.75,$$

where θ is the polar angle of the cluster.

- Each event was divided into two hemispheres by a plane perpendicular to the thrust axis. An invariant mass was calculated from the momenta of the charged tracks and the energy of the lead glass clusters for each hemisphere assuming massless particles. The sum of the invariant masses of the two hemispheres was required to be larger than 3.5 GeV.
- The charged track multiplicity in at least one of the thrust hemispheres was required to be 2 or more.

The factor 1/3 for the forward detector energy in the total energy cut was introduced to optimize the rejection of two-photon events. Figure 3 shows, for the events that pass all other selection cuts, $\sum E_{fdet}$ versus $\sum E_{clus}$ for the OPAL data and for a Monte Carlo simulation of hadronic and leptonic events. The region excluded by the cut is indicated by the solid line. In Figure 3 a) there is a clear excess in this region coming from two-photon events.

The distribution of the energy deposited in the electromagnetic calorimeter showed a clear systematic shift in scale between Monte Carlo and data (see Figure 3 c), and the cluster and track multiplicity distributions showed an offset of the Monte Carlo with respect to the data. Possible errors in the acceptance calculation, resulting from these discrepancies, were estimated by calculating the acceptance after rescaling the electromagnetic energy response in the Monte Carlo, and after offsetting the Monte Carlo multiplicities. Furthermore, cuts were varied over reasonable intervals in order to quantify the effects of possible local distortions in the distributions of the cut variables. These studies resulted in an estimated uncertainty of 0.14% on the acceptance, which was attributed to shortcomings in the detector simulation.

The main contamination in the hadronic data sample came from $\tau^+\tau^-$ and two-photon multi-hadronic events. For $\tau^+\tau^-$ events, a background fraction of $(0.17 \pm 0.01)\%$ was estimated by using Monte Carlo events generated with the KORALZ program, which reproduced well the data distributions. For example, Figure 4 shows the sum of the invariant masses of the two hemispheres after all other cuts have been applied. The small differences observed between data and Monte Carlo in this distribution were taken into account in the estimate of the 0.01% systematic uncertainty. The majority of non-resonant background events are characterized by low visible energy $\sum E_{clus}/\sqrt{s}$ or high longitudinal momentum imbalance $|\sum(E_{clus} \cos \theta)|/\sum E_{clus}$. The background from non-resonant processes was estimated from the data by comparing for each beam energy the cross-sections of events with low and high visible energy and, alternatively, the cross sections of events with high and low longitudinal momentum imbalance. This resulted in a background estimate of 0.064 ± 0.017 nb, corresponding to approximately 0.2% of the cross section at the peak energy point.

A number of alternative selection criteria were used to check the selection described above. The number of events and the overlap of the selected samples were checked and no significant fill-to-fill variations were observed. The cross sections as a function of energy for the selections compared were identical at the level of 0.1%.

It was found that the data contained more energy deposits in the forward detector than the Monte Carlo. These were considered to be due to accidental hits in the forward detector by some beam-related background particles. Possible errors coming from such accidental hits were checked by comparing this selection to the event selection criteria used in our previous publication [1], which does not use the forward detector clusters. The cross section for events which passed the new selection but not the old was compared to that of events which passed both selections at each energy point. This allowed the separation of the resonant and non-resonant components of the exclusive sample. The resonant component was found to agree with the Monte Carlo expectation to within the 0.05% statistical sensitivity of our test. The non-resonant component was also in good agreement with the estimate given above and showed no indication of a possible further systematic uncertainty.

The effect of uncertainties resulting from the modelling of fragmentation was investigated in two ways. We compared the acceptance calculated using the JETSET model with that obtained using the HERWIG model. We observed a difference of 0.06%. We also repeated the acceptance calculation with the JETSET model independently varying each of the optimized parameters of the model by one standard deviation. This resulted in a maximum acceptance change of $(0.09 \pm 0.03)\%$. The differences revealed by these two studies were added in quadrature to give a total systematic error due to the

fragmentation model of 0.11%.

The reconstruction program fails for 0.05% of the events tagged as hadronic events by an online filter algorithm [17], while less than 0.01% of the events tagged as luminosity Bhabha events are missing in the final sample. As this may lead to a systematic shift in the cross section calculation, we assigned a 0.05% systematic error for reconstruction failures.

The full set of correction factors and the corresponding systematic uncertainties are summarized in Table 2. The overall correction factor for the peak energy point was 1.0010, with a systematic uncertainty of 0.20%. The hadronic cross section results are given in Table 6.

5 The Leptonic Decay Channels

The analysis of leptonic final states was performed using techniques very similar to those described in our previous publication [1]. Events were required to lie within the angular range $|\cos\theta| < 0.70$, $|\cos\theta| < 0.95$ and $|\cos\theta| < 0.90$ for the e^+e^- , $\mu^+\mu^-$ and $\tau^+\tau^-$ channels, respectively. The factors by which the selected numbers of candidate events were corrected in order to account for experimental efficiency and background are given in Tables 3, 4 and 5, for electron, muon and tau pairs, respectively. The leptonic cross sections are given in Table 7. In the case of muon and tau pairs the total production cross section is quoted. Corrections for the selection efficiency and geometrical acceptance were evaluated using Monte Carlo events generated with the KORALZ program. In the case of electron pairs the cross section is quoted within the geometrical acceptance and acollinearity cuts, corrected for selection inefficiency and backgrounds.

For the measurement of the forward-backward asymmetry, events were required to have acollinearity angles of less than 10° for the e^+e^- channel and less than 15° for the $\mu^+\mu^-$ and $\tau^+\tau^-$ channels. For the $\mu^+\mu^-$ and $\tau^+\tau^-$ channels the forward-backward asymmetry was calculated using an unbinned maximum likelihood fit to the angular distribution. This was checked by simply counting the numbers of forward and backward events. For the e^+e^- channel, in the absence of a convenient parametrization for the differential cross section, the forward-backward asymmetry was calculated with the simple counting method. The measured forward-backward asymmetries within the geometrical acceptance are given in Tables 8, 9 and 10, for electron, muon and tau pairs, respectively. The numbers of events used in the asymmetry measurements are larger than for the cross sections since less stringent requirements on the status of the detector were needed. This was because a precise knowledge of neither the absolute selection efficiency nor the luminosity was required for the asymmetry analysis.

The increased data sample collected in 1991 allowed the systematic studies described in [1] to be repeated with increased precision. A number of new studies were performed. This, together with continual improvements made in both the performance and understanding of the OPAL detector, is reflected in the reduced systematic errors given in the Tables. In the following three sections we describe briefly the most significant improvements for each leptonic channel.

5.1 The e^+e^- Channel

For this channel, the selection criteria remained essentially unchanged since the analysis of the 1990 data [1]. Events were required to contain two electron candidates with an acollinearity of less than 10° . The negatively charged electron was required to satisfy $|\cos\theta| < 0.70$. Cuts on the number of

tracks, the number of clusters and the total energy of clusters in the electromagnetic calorimeter were used to reject background from hadronic events and tau pairs.

The dominant systematic error quoted in [1] was due to the uncertainty in determining the edge of the geometrical acceptance. We studied the possible effects of local distortions in the reconstructed electromagnetic calorimeter cluster position, the effect of an event vertex displacement, and the consistency of the θ -measurement using calorimeter clusters with that using charged tracks. Furthermore, a comparison was made of the accepted number of events for samples obtained by imposing the geometrical acceptance cuts on the polar angle of the e^- , the polar angle of the e^+ , or a random mixture of both. From these studies, the error due to the uncertainty on the edge of the acceptance was reduced to 0.30%.

The largest correction was applied to account for a small inefficiency for finding charged tracks associated to the calorimeter clusters of the electrons. In this context, candidate events for the process $e^+e^- \rightarrow \gamma\gamma$ were checked. Event samples were isolated which consisted both of true $e^+e^- \rightarrow \gamma\gamma$ and of $e^+e^- \rightarrow e^+e^-$ in which one or more tracks were missed. The causes of missing tracks in $e^+e^- \rightarrow e^+e^-$ events were studied in detail. Based on this study, an additional 0.20% tracking inefficiency correction was applied to the Monte Carlo estimate of 0.45% which gave a total correction of $(0.65 \pm 0.25)\%$.

In order to check the inefficiency due to the calorimeter energy cuts and the level of background from $e^+e^- \rightarrow \tau^+\tau^-$, we examined distributions of calorimeter energy, visible energy and acoplanarity. The electromagnetic calorimeter contains no gaps that point to the interaction region. However, in small regions at the edge of calorimeter modules, showers traverse a smaller amount of lead glass than normal and therefore deposit less energy. The effect of these regions on the visible energy distribution was studied in detail. We estimated the energy cut inefficiency to be $(0.35 \pm 0.12)\%$. This estimate of the inefficiency was 0.20% higher than that predicted by the Monte Carlo, which was corrected accordingly.

The full set of correction factors, valid within the restricted angular range of $|\cos\theta| < 0.7$, and the corresponding systematic uncertainties are summarized in Table 3. The overall correction factor for the peak energy point, within the geometrical acceptance, was 1.0075 with a systematic uncertainty of 0.45%.

The sign of the charge of the particles was determined from tracks in the central detector. A small fraction ($\approx 2\%$) of the events had the same sign measured for both tracks. For these events, an alternative method of charge determination was adopted, using the acoplanarity between the two calorimeter clusters of the e^+e^- pair. With this method, the correct charge assignment was made for approximately 95% of events in the sample, independent of the tracking information. In this way we could use all the $e^+e^- \rightarrow e^+e^-$ events for the asymmetry measurement without rejecting the same sign pairs, thus avoiding any possible bias. Other sources of possible bias on the forward-backward asymmetry measurement were investigated using similar methods to those used for the study of the definition of the geometrical acceptance, described above. As a result of these studies, we assign an uncertainty of 0.003 to the asymmetry measurement for the process $e^+e^- \rightarrow e^+e^-$.

5.2 The $\mu^+\mu^-$ Channel

Muon pairs were selected within the angular range $|\cos\theta| < 0.95$. The main improvement to the selection criteria since our previous publication [1] was to tighten the requirement on the number of charged tracks reconstructed in the central detector. After applying algorithms to recognize photon conversions and tracks which were incorrectly split in the reconstruction, events were required to

contain two or three tracks. In our previous analysis these algorithms were not applied and events were allowed to contain as many as five tracks.

We have significantly reduced the two dominant systematic errors, which in the previous publication [1] came from track reconstruction problems in the regions close to the sense wire planes in the jet chamber, and from the estimation of the residual background from tau pair events.

We performed a search for $e^+e^- \rightarrow \mu^+\mu^-$ events that failed our standard selection cuts because of track reconstruction problems. To do this a second selection algorithm was used, which mainly relied on information from the outer detectors and was almost independent of the central tracking. The selection required back-to-back tracks in the muon chambers and back-to-back clusters in the electromagnetic calorimeter. The time-of-flight counters were used to reject cosmic rays. The purity of the event sample selected by the algorithm was 95% and the selection efficiency for $e^+e^- \rightarrow \mu^+\mu^-$ decays in the OPAL data was 72%.

Overall, we found that 1.05% of muon pairs were lost because of track reconstruction problems in the OPAL data, whereas the Monte Carlo predicted a 0.72% loss. We observed a discrepancy between data and Monte Carlo in the angular distribution of the muon pair events that were lost by the standard selection and found by our tracking-independent algorithm. In the very forward direction the Monte Carlo appeared to overestimate the number of lost events, whereas everywhere else it underestimated the losses. We assigned an error of $\pm 0.11\%$ because of this difference. In summary, we applied a correction of $(-0.33 \pm 0.11)\%$ to the Monte Carlo estimate of the $e^+e^- \rightarrow \mu^+\mu^-$ selection efficiency to account for the observed discrepancy in the track reconstruction efficiency.

In order to check the predicted background from $e^+e^- \rightarrow \tau^+\tau^-$ we studied distributions in visible energy, acoplanarity and acollinearity, that discriminated between $e^+e^- \rightarrow \mu^+\mu^-$ and the backgrounds. For example, we made a selection of muon pair events with an acoplanarity of greater than 10 mrad that could not be explained by the presence of a radiated photon. Combining the 1990 and 1991 OPAL data samples we found 184 such events. This compared well with the Monte Carlo prediction of 175 events, of which 24 were $e^+e^- \rightarrow \mu^+\mu^-$ and 151 $e^+e^- \rightarrow \tau^+\tau^-$ events. This number represented 61% of the total predicted $e^+e^- \rightarrow \tau^+\tau^-$ background in the final sample. As a result of these checks we estimated a background of $(1.15 \pm 0.15)\%$ from $e^+e^- \rightarrow \tau^+\tau^-$.

Events containing four fermions in the final state fail the cut on track multiplicity if the masses of both fermion pairs are large. Since four fermion events are not generated by the KORALZ program this causes the selection efficiency calculated with the Monte Carlo to be overestimated. From a visual inspection of all events that failed only the multiplicity cut we assigned a systematic error of 0.05% to account for this effect.

The remaining, less significant, uncertainties given in Table 4 similarly profited from the improved systematic checks we were able to perform on the increased data samples now available. The full set of correction factors and the corresponding systematic uncertainties are summarized in Table 4. The overall correction factor for the peak energy point was 1.0890, with a systematic uncertainty of 0.25%.

For the forward-backward asymmetry measurement events were required to have exactly two oppositely charged tracks; 1.2% of $\mu^+\mu^-$ events were rejected by this requirement. In order to ensure that the polar angle of tracks in the barrel region of the detector was reliably measured, matches to hits in both the z-chambers and the stereo wires of the vertex drift chamber were required. If this criterion was not satisfied, but the track was matched to hits in the barrel muon chambers then the position of these hits, under the assumption that the track originated from the nominal e^+e^- interaction point, was used to determine the polar angle. In 0.3% of the event sample the polar angle of neither track could be reliably determined and these events were not used in the asymmetry measurement.

The measurement was checked by using only positive tracks, only negative tracks, or using a track of randomly chosen charge to measure the asymmetry. The acoplanarity measured in the muon chambers was used as an alternative way to determine the charge of the muons, and compared to the results of the tracking method. Additional checks were performed by varying the cuts on the quality of central detector tracks used in the asymmetry measurement. As a result of these checks we assigned an uncertainty of 0.003 on the asymmetry measurement for muon pairs.

5.3 The $\tau^+\tau^-$ Channel

Z^0 decays to tau pairs were selected within the angular range $|\cos\theta| < 0.90$ using criteria that remained unchanged since our last publication [1].

The uncertainty in the determination of the edge of the acceptance had been one of the dominant systematic errors. Consistency checks between data and Monte Carlo were performed by comparing the number of accepted events when tracks only, clusters only or both tracks and clusters were used to reconstruct the direction of the $\tau^+\tau^-$ pair. As a result of this study, the uncertainty on the definition of the geometrical acceptance was reduced to 0.39%. Most of the systematic errors assigned to the efficiency of the selection criteria within the geometrical acceptance have been reduced because of the availability of larger samples of data and Monte Carlo, leading to a total uncertainty of 0.42%. These errors were determined by comparing the distributions of cut variables in data and Monte Carlo in order to allow for possible discrepancies in the vicinity of the cuts.

Backgrounds were checked by selecting subsamples of the candidate tau pair events in which the background fraction of a given source was enhanced. By applying more effective cuts than in our previous publication, these searches for backgrounds were less sensitive to the statistical error from the genuine tau pairs included in the subsamples under study.

Hadronic background events were tagged by requiring one of the jets in tau pair candidate events to have a large multiplicity. Good agreement was observed between data and Monte Carlo for the multiplicity distribution of the jet opposite the tag. Using this technique, we have assigned a systematic uncertainty of 0.29% on the level of hadronic background in the tau pair sample.

Residual backgrounds from $\mu^+\mu^-$ and e^+e^- events were studied by isolating the subset of events in which at least one tau jet had large energy which was consistent with the beam energy. These studies also made use of the small acoplanarity angle typical of $\mu^+\mu^-$ and e^+e^- events. Backgrounds due to $\mu^+\mu^-$ and e^+e^- could be differentiated in these samples by the electromagnetic energy distributions of the two jets in the event. As a result of these studies, the systematic uncertainties on the background from e^+e^- and $\mu^+\mu^-$ were both estimated to be 0.19%.

Backgrounds from non-resonant processes were checked by using the direction of the missing momentum vector and were found to be consistent with the Monte Carlo prediction to within 0.17%.

The full set of correction factors and the corresponding systematic uncertainties are summarized in Table 5. The overall correction factor for the peak energy point was 1.3001, with a systematic uncertainty of 0.76%.

For about 2.1% of the events in the $\tau^+\tau^-$ sample an unambiguous charge assignment could not be made. These events were excluded from the forward-backward asymmetry measurement. Possible biases to the forward-backward asymmetry measurement were examined by comparing the results when tracks only, clusters only or both tracks and clusters were used to reconstruct the direction of

the $\tau^+\tau^-$ pair. We also compared the results obtained using the direction of the τ^+ , the τ^- or the average of the two. As a result of these studies, we estimated an uncertainty of 0.003 on the asymmetry measurement for tau pairs.

5.4 Correlation of Systematic Errors Among the Three Leptonic Channels

The three leptonic samples were defined to be complementary in the region of common geometrical acceptance. By so doing, no additional uncertainty with respect to an inclusive charged lepton analysis is introduced, even once the assumption of lepton universality is made. Keeping separate $e^+e^- \rightarrow e^+e^-$, $e^+e^- \rightarrow \mu^+\mu^-$ and $e^+e^- \rightarrow \tau^+\tau^-$ samples, however, allowed us to optimize the treatment of each channel. The complementarity of the leptonic samples leads to an anticorrelation of the uncertainty due to cross-over of events from one leptonic channel into another. These anticorrelated uncertainties, which must be taken into account when comparing our cross-sections to the hypothesis of lepton universality, were 0.24% between the $\mu^+\mu^-$ and $\tau^+\tau^-$ samples and 0.21% between the e^+e^- and $\tau^+\tau^-$ channels. There was no significant anticorrelated error between the $\mu^+\mu^-$ and e^+e^- channels and there were no significant correlated uncertainties for the acceptance corrections among the three channels.

6 LEP Energy Calibration

A precise calibration of the LEP energy scale was achieved in 1991 [2]. This was based on the technique of resonant depolarization of a transversely polarized electron beam, as well as on detailed studies of the properties of the LEP magnets and RF system. The fractional uncertainty in the overall energy scale was reduced from $\pm 22 \cdot 10^{-5}$ in 1990 to $\pm 5.7 \cdot 10^{-5}$ for the data taken during the energy scan around the Z^0 resonance in the second half of 1991. The energy of the data taken at the Z^0 peak in the first half of 1991, before the polarization calibration was available, had a larger fractional uncertainty of $\pm 20 \cdot 10^{-5}$. This calibration cannot be applied retrospectively to the 1990 measurements.

In our analysis, LEP fills with a nominal centre-of-mass energy within 10 MeV of each other were combined into one ‘scan point’. In 1991 about 120 fills were taken at an energy close to the peak of the Z^0 resonance and five fills at each one of the six off-peak points. The fill-to-fill reproducibility of the energy was given as $\pm 10 \cdot 10^{-5}$. There was a correlated uncertainty between the energies E_i of scan points introduced through a local energy scale error in the extrapolation of the energy measurement by resonant depolarization at an energy of 93 GeV to other energies, described by $\pm 1.5 \cdot 10^{-3}(93 \text{ GeV} - E_i)$. Systematically different settings of machine parameters at the different scan points could have led to small energy changes with respect to the nominal energy, estimated to be $\pm 3 \cdot 10^{-5}$.

In the light of a better understanding of the energy calibration, corrections have been applied to our published 1990 energies. The geometry of the LEP radio-frequency accelerating cavities introduced a shift of $+16 \pm 2$ MeV in centre-of-mass energy at the OPAL interaction point relative to the values used in [1]. A non-linearity correction of $(1.9 \pm 1.5) \cdot 10^{-3}(91.2 \text{ GeV} - E_i)$ was applied to the 1990 scan points. All errors were taken into account by constructing the error correlation matrix between the scan points in 1991 and 1990. The point-to-point setting error and the uncertainty of the non-linearity correction were assumed to be fully correlated between 1990 and 1991.

The spread of the centre-of-mass energy of 51 ± 5 MeV, due to the energy spread of particles in the beams, was taken into account by correcting the measured cross sections in the fitting procedure

using the Taylor expansion:

$$\Delta\sigma(E) \approx -\frac{1}{2} \frac{d^2\sigma(E)}{dE^2} \Delta E^2.$$

The effect of this correction amounts to a change in the cross section at $\sqrt{s} = M_Z$ by +0.14% and a change in Γ_Z by -4 MeV, but has a negligible effect on other quantities as compared to their statistical errors.

7 Determination of Electroweak Parameters

Electroweak parameters were determined from the measurements described in the previous sections (Tables 6-10), our published 1990 hadronic and leptonic cross sections (Tables 7-10 in reference [1]) and our combined 1989/1990 leptonic asymmetries (Tables 11-13 of reference [1]). The procedure used to fit the cross sections and the leptonic asymmetries was essentially the same as that described in our previous publication [1]. Parameters were obtained using a χ^2 minimization procedure taking into account the full covariance matrix of the data. The systematic errors of the 1990 measurements were in general larger than those of 1991. The 1991 systematic errors were treated as common uncertainties between 1990 and 1991. The systematic checks on the absolute luminosity measurement for the 1991 data were considerably improved by the new drift-chamber analysis. We therefore did not include the information from the absolute luminosity measurement in 1990. Technically this was implemented by rescaling our published 1990 cross sections, by a factor of 1.0085, in order to normalize the 1990 hadronic cross section at the Z^0 peak to the 1991 measurement, and by inflating the overall normalization error for the 1990 data. The absolute energy determination for the 1990 data was not used. For the purposes of our fit, the 1990 energies were rescaled by a factor of 1.00024, such that the value obtained for M_Z was the same for the 1990 and 1991 data sets, and the systematic error on the 1990 absolute energy determination was inflated. Hence the determination of M_Z and the cross section at the Z^0 peak are almost completely determined by the 1991 data.

The theoretical parametrizations of the total and differential cross sections for the processes $e^+e^- \rightarrow$ hadrons, $e^+e^- \rightarrow \mu^+\mu^-$, $e^+e^- \rightarrow \tau^+\tau^-$ and the contribution of s -channel diagrams to $e^+e^- \rightarrow e^+e^-$ were obtained with the program ZFITTER [18]. For the process $e^+e^- \rightarrow e^+e^-$ we used the program ALIBABA [19] to describe the contributions from the t -channel diagrams and from s - t interference. These were then added to the s -channel differential cross sections calculated by ZFITTER. Following the recommendation in [19], an uncertainty of 0.5% was assigned to these contributions.

7.1 Extended Improved Born Approach

The total cross section of the hard scattering process $e^+e^- \rightarrow$ hadrons is dominated by the pure Z^0 contribution. Without photonic corrections this contribution can be parametrized by a Breit-Wigner line-shape with an s -dependent width:

$$\sigma(s) = \sigma_{\text{had}}^{\text{pole}} \frac{s\Gamma_Z^2}{(s - M_Z^2)^2 + (s^2/M_Z^2)\Gamma_Z^2}, \quad (1)$$

where $\sigma_{\text{had}}^{\text{pole}}$ represents the hadronic pole cross section at $\sqrt{s} = M_Z$ in the absence of initial state photon radiation. Small additional contributions from γ exchange and from γ - Z^0 interference were calculated within the Standard Model framework. To check that this procedure does not introduce a Standard Model bias, the Standard Model contribution of the γ - Z^0 interference was multiplied by a scale factor

which was treated as a free parameter. We obtained for this scale factor -1.1 ± 3.6 which is in good agreement with unity.

To parametrize the s -channel leptonic differential cross sections we used an extension of the improved Born approximation [20]:

$$\begin{aligned} \frac{2s}{\pi\alpha^2} \frac{d\sigma}{d\cos\theta}(e^+e^- \rightarrow \ell^+\ell^-) &= \left| \frac{1}{1-\Delta\alpha} \right|^2 (1 + \cos^2\theta) \\ &+ 4\text{Re} \left\{ \frac{2}{1-\Delta\alpha} \chi(s) \left[C_{\gamma Z}^s(1 + \cos^2\theta) + 2C_{\gamma Z}^a \cos\theta \right] \right\} \\ &+ 16|\chi(s)|^2 [C_{ZZ}^s(1 + \cos^2\theta) + 8C_{ZZ}^a \cos\theta], \end{aligned} \quad (2)$$

with

$$\chi(s) = \frac{G_F M_Z^2}{8\pi\alpha\sqrt{2}} \frac{s}{s - M_Z^2 + is\Gamma_Z/M_Z}.$$

Here α is the electromagnetic coupling constant and G_F is the Fermi constant. Besides M_Z and Γ_Z the four coefficients $C_{\gamma Z}^s$, $C_{\gamma Z}^a$, C_{ZZ}^s and C_{ZZ}^a are treated as free parameters, where the superscripts ‘ s ’ and ‘ a ’ refer to terms symmetric and antisymmetric in $\cos\theta$. With this parametrization we retain the effective Born structure of the differential cross section, but relax the constraints on the relative strengths of the various contributions that are imposed by a description in terms of vector and axial-vector couplings. This can be seen more clearly by writing the C parameters in terms of effective vector and axial-vector coupling constants, \hat{g}_v and \hat{g}_a , and four scale factors $\kappa_{\gamma Z}^s$, $\kappa_{\gamma Z}^a$, κ_{ZZ}^s and κ_{ZZ}^a . In the improved Born approximation the κ parameters are equal to 1. They are introduced here to allow for a more general approach:

$$\begin{aligned} C_{\gamma Z}^s &\equiv \kappa_{\gamma Z}^s \hat{g}_v^e \hat{g}_v^\ell \\ C_{\gamma Z}^a &\equiv \kappa_{\gamma Z}^a \hat{g}_a^e \hat{g}_a^\ell \\ C_{ZZ}^s &\equiv \kappa_{ZZ}^s (\hat{g}_a^{e2} + \hat{g}_v^{e2})(\hat{g}_a^{\ell2} + \hat{g}_v^{\ell2}) \\ C_{ZZ}^a &\equiv \kappa_{ZZ}^a \hat{g}_a^e \hat{g}_a^\ell \hat{g}_v^e \hat{g}_v^\ell. \end{aligned}$$

The superscripts ‘ e ’ and ‘ ℓ ’ denote electronic and leptonic coupling constants, where ‘ ℓ ’ stands for either electron, muon or tau leptons. The first term in Equation 2 arises from pure QED photon exchange, the second term describes the γ - Z^0 interference, indicated by the subscripts ‘ γZ ’ on the C and κ parameters, and the last term arises from Z^0 exchange, indicated by the subscripts ‘ ZZ ’. Effects from non-photon radiative corrections are accounted for by including the QED vacuum polarization correction $\Delta\alpha$, an s -dependence of the Z^0 width in the propagator, and by using effective vector and axial-vector couplings denoted by \hat{g}_v and \hat{g}_a .

The improved Born parametrization is an approximation since it is based on the assumption that the effective vector and axial-vector couplings are real and energy independent, but otherwise it is model independent. At the present level of accuracy significant deviations of the relative strengths of the various terms from the improved Born prediction could indicate new physics, leading to a break-down of the approximation, due to unexpected higher order corrections or a modification of the Born process. Our approach allows the interpretation of possible deviations from the effective Born relations to be directly related to the experimental measurements. Similar tests can also be performed in a rigorously model independent manner using approaches such as those described in [21].

Table 11 gives the results of fits to the combined data set of hadronic and leptonic cross sections and leptonic forward-backward asymmetries. Parameter correlation matrices are given in the Appendix. The values in the second column of Table 11 were obtained from a 15 parameter fit with M_Z , Γ_Z , $\sigma_{\text{had}}^{\text{pole}}$, and the 12 C parameters ($C_{\gamma Z}^s$, $C_{\gamma Z}^a$, C_{ZZ}^a and C_{ZZ}^s individually for each leptonic species) as free parameters. The values obtained from the different leptonic species for corresponding parameters are consistent with one another, supporting the hypothesis of lepton universality. The most precise test of lepton universality is obtained from the ratio of C_{ZZ}^s parameters for different leptonic species, as the overall normalization error cancels. In the improved Born approximation the ratio of C_{ZZ}^s parameters can be expressed as:

$$R_{\ell/\tau} = \frac{C_{ZZ}^s(\ell^+\ell^-)}{C_{ZZ}^s(\tau^+\tau^-)} \equiv \frac{\hat{g}_a^{\ell^2} + \hat{g}_v^{\ell^2}}{\hat{g}_a^{\tau^2} + \hat{g}_v^{\tau^2}} \quad \text{for } \ell = e \text{ or } \mu.$$

The result of our measurement is:

$$\begin{aligned} R_{e/\tau} &= 1.008 \pm 0.016 \\ R_{\mu/\tau} &= 1.025 \pm 0.014. \end{aligned}$$

Column three of Table 11 gives the results for a 7 parameter model-independent fit when lepton universality was assumed explicitly by imposing $C(e^+e^-) \equiv C(\mu^+\mu^-) \equiv C(\tau^+\tau^-)$ for each of the four C parameters.

Figure 5 shows a comparison of the results with the Standard Model prediction for the fitted parameters. Good agreement is observed for all parameters. The largest deviation is in the parameter $C_{\gamma Z}^a = \kappa_{\gamma Z}^a \hat{g}_a^{\ell^2}$, which differs by two standard deviations from the Standard Model. This deviation is due to the energy-dependence of the forward-backward asymmetry. Strictly speaking the measurement of the off-peak leptonic forward-backward asymmetry determines only the ratio of the parameters $C_{\gamma Z}^a/C_{ZZ}^s$. The relative error on C_{ZZ}^s is, however, negligible compared to the relative deviation of $C_{\gamma Z}^a$ from the Standard Model. The error on $C_{\gamma Z}^a$ is completely dominated by statistics.

The effective leptonic couplings, $\hat{g}_a^{\ell^2}$ and $\hat{g}_v^{\ell^2}$, can be determined by setting all κ factors equal to 1. The result is given in the last row of Table 12 and is consistent with the Standard Model prediction. In principle $\hat{g}_a^{\ell^2}$ and $\hat{g}_v^{\ell^2}$ can be determined from any pair of C parameters; this is illustrated in the upper part of Table 12. It should be noted that the determination from a combined fit to all four C parameters is completely dominated by the precisely measured parameters C_{ZZ}^s and C_{ZZ}^a .

7.2 Derived Parameters

The set of parameters presented in section 7.1 is sufficient to characterize the data. Parameter transformations are, however, useful to emphasize certain aspects of the measurements. In this section we first derive the partial decay widths of the Z^0 to hadrons, Γ_{had} , and to leptons, $\Gamma_{\ell\ell}$, from the parameters of our model independent fit. The leptonic partial decay widths of the Z^0 are related to the parameter $C_{ZZ}^s(\ell^+\ell^-)$ by [§]:

$$C_{ZZ}^s(\ell^+\ell^-) = \left(\frac{6\pi\sqrt{2}}{G_F M_Z^3} \right)^2 \frac{\Gamma_{ee}\Gamma_{\ell\ell}}{\delta_{QED}^2}. \quad (3)$$

[§]For simplicity we neglect small mass terms in the following equations which relate the C coefficients to partial widths. These mass terms were taken into account in the fitting procedure.

The hadronic pole cross section can be expressed in terms of the Z^0 mass, the total width and the partial decay width into hadrons and electrons:

$$\sigma_{\text{had}}^{\text{pole}} = \frac{12\pi}{M_Z^2} \frac{\Gamma_{ee}\Gamma_{\text{had}}}{\Gamma_Z^2}. \quad (4)$$

The factor $\delta_{QED} = 1 + \frac{3}{4}\frac{\alpha}{\pi}$ accounts for the effects of final state radiation which, by convention, is included in the definition of the partial width. The partial decay widths Γ_{had} , Γ_{ee} , $\Gamma_{\mu\mu}$ and $\Gamma_{\tau\tau}$, as given in Table 13, have been obtained by a parameter transformation from the parameters $C_{ZZ}^s(e^+e^-)$, $C_{ZZ}^s(\mu^+\mu^-)$, $C_{ZZ}^s(\tau^+\tau^-)$, M_Z , Γ_Z and $\sigma_{\text{had}}^{\text{pole}}$ from our model independent fit. The leptonic partial widths are consistent with each other, as already observed in the results for the C_{ZZ}^s parameters.

For the decay width of the Z^0 into invisible final states, Γ_{inv} , we obtain:

$$\Gamma_{\text{inv}} = \Gamma_Z - \Gamma_{\text{had}} - 3\Gamma_{\ell\ell} = 495 \pm 10 \text{ MeV},$$

and for the ratio of $\Gamma_{\text{inv}}/\Gamma_{\ell\ell}$:

$$\Gamma_{\text{inv}}/\Gamma_{\ell\ell} = 5.94 \pm 0.12.$$

Combining the measured value of $\Gamma_{\text{inv}}/\Gamma_{\ell\ell}$ with the Standard Model prediction for $\Gamma_{\nu}/\Gamma_{\ell\ell} = 1.992 \pm 0.003$, where the error refers to a variation of the mass of the top quark M_t in the interval $50 < M_t \text{ (GeV)} < 230$ and the mass of the Higgs boson M_H in the interval $60 < M_H \text{ (GeV)} < 1000$, we obtain for the number of light neutrino generations:

$$N_{\nu} = 2.98 \pm 0.06(\text{exp.}) \pm 0.005(M_t, M_H).$$

We also apply a parameter transformation to our model independent fit to describe our data in terms of M_Z , Γ_Z , $\sigma_{\text{had}}^{\text{pole}}$, R_{ℓ} and $A_{\text{FB}}^{\text{pole}}$, where R_{ℓ} is the ratio

$$R_{\ell} \equiv \frac{\Gamma_{\text{had}}}{\Gamma_{\ell\ell}} = \frac{\sigma_{\text{had}}^{\text{pole}}}{C_{ZZ}^s(\ell^+\ell^-)} \frac{1}{\delta_{QED}^2} \frac{\Gamma_Z^2}{M_Z^4} \frac{6\pi}{G_F^2},$$

and $A_{\text{FB}}^{\text{pole}}$ is the leptonic forward-backward asymmetry at the pole,

$$A_{\text{FB}}^{\text{pole}} = 3 \frac{C_{ZZ}^a}{C_{ZZ}^s}.$$

This parameter set is closely related to the experimental measurements and correlations between these parameters are small. Furthermore it has been adopted by the four LEP experiments to facilitate the comparison of measurements. The results of the model independent fit expressed in terms of these parameters are given in Table 14. Parameter correlation matrices are given in the Appendix. Figure 6 shows, for each leptonic species, the resulting one standard deviation contours in the R_{ℓ} - $A_{\text{FB}}^{\text{pole}}$ plane. The comparison of the R_{ℓ} values for the individual leptonic species provides a test of lepton universality with similar sensitivity to the ratio of C_{ZZ}^s parameters, as the overall normalization error cancels in R_{ℓ} . These results are again compatible with lepton universality.

7.3 Standard Model Fits

In this section we compare the data to the Standard Model prediction and infer constraints on the model's unknown input parameters. Since the fine structure constant, α , and the Fermi constant, G_F , are precisely measured, we treat as the free parameters of the Standard Model prediction M_Z , the mass of the top quark M_t , the mass of the Higgs boson M_H and the strong coupling constant $\alpha_s(M_Z^2)$,

where the latter three parameters enter through radiative corrections. To parametrize our data, we used the full one-loop Standard Model calculation provided in the program ZFITTER, which includes leading $\mathcal{O}(\alpha^2 M_t^4)$ and $\mathcal{O}(\alpha\alpha_s)$ terms. QCD corrections were calculated to $\mathcal{O}(\alpha_s^3)$ and include quark mass dependent corrections [22]. From the fit to our data we obtain:

$$\begin{aligned} M_Z &= 91.182 \pm 0.007 \pm 0.006 \text{ GeV} \\ M_t &= 91_{-...}^{+46} \pm 9 \text{ GeV} \\ \alpha_s(M_Z^2) &= 0.135 \pm 0.015 \pm 0.002, \end{aligned}$$

with a $\chi^2/\text{NDOF}=69.0/102$. The central values of M_t and $\alpha_s(M_Z^2)$ refer to a fixed value of $M_H = 300$ GeV. The second error shows the variation of the central value for Higgs masses spanning the interval $60 < M_H(\text{GeV}) < 1000$. The dots for the lower bound on M_t indicate that the error extends beyond the threshold for open top production ($M_t < M_Z/2$), which is excluded by direct searches and not implemented in our parametrization. In the context of the Standard Model our measurements lead to a value of $M_W = 79.87_{-0.21}^{+0.26} \pm 0.04$ GeV (imposing $M_t > M_Z/2$) in good agreement with the direct measurements of CDF and UA2 [23] and of similar precision. The fitted value for $\alpha_s(M_Z^2)$ is determined from the ratio $R_\ell = \Gamma_{\text{had}}/\Gamma_{\ell\ell}$ and the total width Γ_Z . The value we obtain is consistent with the OPAL values [24], $\alpha_s(M_Z^2) = 0.122_{-0.006}^{+0.005}$, determined from event topologies, jet rates and energy correlations and, $\alpha_s(M_Z^2) = 0.123_{-0.007}^{+0.006}$, determined from τ decays. If we calculate $\alpha_s(M_Z^2)$ from R_ℓ alone, we obtain for $M_t=150$ GeV and $M_H=300$ GeV, $\alpha_s(M_Z^2) = 0.139 \pm 0.020(\text{exp.})_{-0.005}^{+0.006}$, where the second error reflects the variation of our result for the M_t and M_H ranges quoted above.

Figures 7 and 8 show comparisons of the measured cross sections and asymmetries with the result of the Standard Model fit. We observe excellent agreement between the data and the result of the fit. The largest deviation is in the distribution of the residuals of the energy-dependence of the forward-backward asymmetry for leptons (see Figure 8 d). This leads to the previously discussed two standard deviation difference of the parameter $C_{\gamma Z}^a$ from the Standard Model prediction.

Figure 9 shows the χ^2 -curves, as a function of M_t , for the direct Standard Model fit to the corrected cross sections and forward-backward asymmetries. From these χ^2 -curves we derive an upper limit on M_t of:

$$M_t < 180 \text{ GeV at } 95\% \text{ CL.}$$

Alternatively M_t can be determined from a fit to the model independent parameters given in section 7.1. As indicated in Figure 9 these fits differ in the region of the minimum of χ^2 , however they both result in approximately the same upper confidence limit for M_t .

8 Summary and Conclusions

Based on a total of 454 300 $e^+e^- \rightarrow \text{hadrons}$, 17 000 $e^+e^- \rightarrow e^+e^-$, 22 700 $e^+e^- \rightarrow \mu^+\mu^-$ and 18 200 $e^+e^- \rightarrow \tau^+\tau^-$ events, we have measured a value of $M_Z = 91.181 \pm 0.007 \pm 0.006$ GeV and $\Gamma_Z = 2.483 \pm 0.011 \pm 0.004$ GeV, where the first error is essentially statistical and the second refers to the uncertainty in the LEP energy scale.

We have performed a model independent analysis of Z^0 parameters based on an extension of the improved Born approximation. Comparing the resulting parameters with the Standard Model prediction we observe good agreement. The largest deviation is in the energy dependence of the leptonic forward-backward asymmetry, which differs by two standard deviations from the Standard Model prediction.

Several observables that test lepton universality have been presented and show agreement with this hypothesis.

From a fit of the Standard Model prediction to our data we derive an upper limit on the top quark mass of $M_t < 180$ GeV at the 95% confidence limit. The strong coupling constant determined from this fit is $\alpha_s(M_Z^2) = 0.135 \pm 0.015 \pm 0.002$, in good agreement with results derived from event topologies, jet rates, energy correlations and τ decays.

Our results are consistent with those of the other LEP Collaborations [25].

Acknowledgements

We are grateful to D. Bardin, W. Beenakker, F.A. Berends, M. Bilenky, S. Jadach, R. Kleiss, J.H. Kühn, S.C. van der Marck, T. Riemann, M. Sachwitz and Z. Was for their help and advice concerning the programs and the analytic formulae used in this analysis.

It is a pleasure to thank the SL Division for the efficient operation of the LEP accelerator, the precise information on the absolute energy, and their continuing close cooperation with our experimental group. In addition to the support staff at our own institutions we are pleased to acknowledge the Department of Energy, USA, National Science Foundation, USA, Science and Engineering Research Council, UK, Natural Sciences and Engineering Research Council, Canada, Israeli Ministry of Science, Minerva Gesellschaft, Japanese Ministry of Education, Science and Culture (the Monbusho) and a grant under the Monbusho International Science Research Program, American Israeli Bi-national Science Foundation, Direction des Sciences de la Matière du Commissariat à l'Énergie Atomique, France, Bundesministerium für Forschung und Technologie, FRG, National Research Council of Canada, Canada, A.P. Sloan Foundation and Junta Nacional de Investigação Científica e Tecnológica, Portugal.

Source of Uncertainty	Uncertainty
8 'Telescope' study	0.30 %
drift chamber survey of tubes	0.21 %
simulation systematics	0.20 %
locations of drift wires	0.10 %
tube pitch	0.08 %
using 1992 survey for 1991	0.06 %
distance to interaction point	0.04 %
calorimeter coordinates	0.04 %
trigger inefficiency	<0.02 %
reconstruction inefficiency	<0.01 %
accidental background	<0.01 %
data statistics	0.32 %
Monte Carlo statistics	0.24 %
overall	0.60 %

Table 1: Summary of experimental uncertainties in the 1991 absolute luminosity analysis.

	Correction Factor	Uncertainty [%]
Acceptance/Efficiency:		
$e^+e^- \rightarrow$ hadrons Monte Carlo	1.0048	0.04
quality of detector simulation	1.0000	0.14
reconstruction failures	1.0000	0.05
Background:		
$e^+e^- \rightarrow \tau^+\tau^-$	0.9983	0.01
non-resonant background (0.064 ± 0.017 nb)	0.9979	0.06
forward detector accidental hits	1.0000	0.05
Theoretical error:		
fragmentation	1.0000	0.11
overall	1.0010	0.20

Table 2: Summary of the correction factors and systematic errors for the 1991 hadronic cross section calculation. In addition there is a correlated point-to-point systematic uncertainty to account for a possible energy dependence of the Monte Carlo correction factor of $0.2\% \cdot |\Delta E|/3$, where ΔE is the difference in energy in GeV, from the point at the peak of the Z^0 resonance.

	Correction Factor	Uncertainty [%]
Acceptance/Efficiency:		
edge of acceptance	1.0000	0.30
calorimeter energy cut	1.0035	0.12
tracking inefficiency	1.0065	0.25
trigger efficiency	1.0000	$\ll 0.10$
Background:		
$e^+e^- \rightarrow \tau^+\tau^-$	0.9975	0.15
$e^+e^- \rightarrow \text{hadrons}$	1.0000	< 0.05
$e^+e^- \rightarrow \gamma\gamma$	1.0000	< 0.05
$e^+e^- \rightarrow e^+e^-e^+e^-$	1.0000	< 0.05
overall	1.0075	0.45

Table 3: Summary of the correction factors and systematic errors for the 1991 $e^+e^- \rightarrow e^+e^-$ cross section calculation. The correction factors listed apply to the restricted angular range of $|\cos\theta| < 0.7$ used for this analysis.

	Correction Factor	Uncertainty [%]
Acceptance/Efficiency:		
$e^+e^- \rightarrow \mu^+\mu^-$ Monte Carlo	1.0981	0.09
muon identification	1.0008	0.04
tracking losses	1.0033	0.11
trigger efficiency	1.0012	0.04
edge of geometrical acceptance	1.0000	0.10
cut on number of tracks	1.0000	0.05
treatment of four-fermion events	1.0000	0.05
only one final-state photon in KORALZ	1.0000	< 0.05
online filter efficiency	1.0000	< 0.05
cosmic ray rejection using TOF/vertex	1.0000	< 0.05
Background:		
$e^+e^- \rightarrow \tau^+\tau^-$	0.9885	0.15
cosmic rays	0.9980	0.05
$e^+e^- \rightarrow e^+e^-\mu^+\mu^-$	1.0000	< 0.05
overall	1.0890	0.25

Table 4: Summary of the correction factors and systematic errors for the 1991 $e^+e^- \rightarrow \mu^+\mu^-$ cross section calculation. Note that the effects ‘muon identification’, ‘tracking losses’ and ‘cut on number of tracks’ were, in principle, simulated by the Monte Carlo. The quoted corrections were introduced to take into account the observed discrepancies between the data and Monte Carlo for these effects.

	Correction Factor	Uncertainty [%]
Acceptance/Efficiency:		
$e^+e^- \rightarrow \tau^+\tau^-$ Monte Carlo	1.3327	0.19
τ -pair selection cuts	1.0000	0.42
definition of $ \cos\theta $	1.0000	0.39
vertex cut	1.0000	0.09
treatment of four-fermion events	1.0000	0.05
time-of-flight efficiency	1.0000	<0.01
trigger efficiency	1.0006	0.06
uncertainty of tau branching fraction	1.0000	<0.05
Background:		
$e^+e^- \rightarrow$ hadrons	0.9961	0.29
$e^+e^- \rightarrow e^+e^-$	0.9950	0.19
$e^+e^- \rightarrow \mu^+\mu^-$	0.9901	0.19
cosmic rays and beam-gas events	0.9983	0.13
two-photon reactions (5.20 ± 1.95 pb)	0.9954	0.17
overall	1.3001	0.76

Table 5: Summary of the correction factors and systematic errors for the 1991 $e^+e^- \rightarrow \tau^+\tau^-$ cross section calculation.

\sqrt{s} (GeV)	Luminosity (nb ⁻¹)	N_{had}	σ_{had} (nb)
91.254	5146	156592	30.46 ± 0.10
88.481	682	3646	5.35 ± 0.10
89.472	790	7991	10.13 ± 0.13
90.227	875	16011	18.32 ± 0.17
91.223	3022	92025	30.48 ± 0.13
91.969	825	20353	24.69 ± 0.22
92.968	593	8356	14.11 ± 0.18
93.717	946	9404	9.95 ± 0.12
Total	12879	314378	

Table 6: The 1991 hadronic cross section, σ_{had} , as a function of the luminosity-weighted centre-of-mass energy, \sqrt{s} . Listed are also the integrated luminosity and the number of observed hadronic events, N_{had} . The cross sections are quoted with their statistical and point-to-point systematic uncertainty of both the hadronic acceptance and the luminosity calculation. The first energy point corresponds to the data which was accumulated at a fixed centre-of-mass energy during the first half of 1991. The remainder was recorded during scans of seven energy points around the Z^0 mass.

\sqrt{s} (GeV)	σ_{ee} (nb)	$\sigma_{\mu\mu}^{\text{tot}}$ (nb)	$\sigma_{\tau\tau}^{\text{tot}}$ (nb)
91.254	0.991±0.014	1.490±0.018	1.436±0.019
88.481	0.364±0.024	0.233±0.020	0.278±0.023
89.472	0.565±0.028	0.519±0.027	0.486±0.029
90.227	0.765±0.030	0.912±0.035	0.836±0.036
91.223	1.013±0.019	1.491±0.023	1.442±0.025
91.969	0.691±0.030	1.249±0.042	1.192±0.044
92.968	0.418±0.027	0.686±0.035	0.697±0.040
93.717	0.303±0.018	0.481±0.024	0.500±0.027

Table 7: The 1991 leptonic cross sections without systematic errors, from a total of 10 736 $e^+e^- \rightarrow e^+e^-$ events, 14 855 $e^+e^- \rightarrow \mu^+\mu^-$ events and 11 507 $e^+e^- \rightarrow \tau^+\tau^-$ events. σ_{ee} is the cross section measured within the angular acceptance $|\cos\theta| < 0.7$ and the acollinearity angle less than 10° , corrected for the effects of efficiency. $\sigma_{\mu\mu}^{\text{tot}}$ and $\sigma_{\tau\tau}^{\text{tot}}$ are the total cross sections after correction for efficiency and acceptance for a cut on the mass of the final state fermion pair $\sqrt{s'} > 0.01\sqrt{s}$.

\sqrt{s} (GeV)	N_F^{ee}	N_B^{ee}	A_{FB}^{ee}
91.254	3061	2563	0.089±0.013
88.479	218	79	0.469±0.051
89.469	287	164	0.274±0.045
90.227	403	280	0.181±0.038
91.220	1860	1505	0.106±0.017
91.969	316	250	0.117±0.042
92.968	175	150	0.077±0.055
93.717	150	134	0.057±0.059

Table 8: The 1991 forward-backward asymmetry corrected for background for the process $e^+e^- \rightarrow e^+e^-$ within the angular acceptance $|\cos\theta| < 0.7$ and the acollinearity angle less than 10° , from a total of 11 595 events. The systematic error of the measurements is 0.003.

\sqrt{s} (GeV)	$N_F^{\mu\mu}$	$N_B^{\mu\mu}$	$A_{FB}^{\mu\mu}$ (Counting)	$A_{FB}^{\mu\mu}$ (Fitting)
91.254	3795	3768	0.004±0.011	0.002±0.011
88.480	70	106	-0.205±0.074	-0.228±0.070
89.472	164	199	-0.096±0.052	-0.106±0.050
90.227	344	400	-0.075±0.037	-0.069±0.034
91.224	2180	2242	-0.014±0.015	-0.022±0.014
91.969	454	462	-0.009±0.033	0.002±0.031
92.968	275	203	0.151±0.045	0.152±0.042
93.717	219	185	0.084±0.050	0.085±0.046

Table 9: The 1991 forward-backward asymmetry for $e^+e^- \rightarrow \mu^+\mu^-$ within $|\cos\theta| < 0.95$ and the acollinearity angle less than 15° , from a total of 15 066 events. The systematic error of the measurements is 0.003. The forward-backward asymmetries in column four were obtained from the numbers in columns two and three; column five represents the results from a maximum likelihood fit to the $\cos\theta$ distribution.

\sqrt{s} (GeV)	$N_{\text{F}}^{\tau\tau}$	$N_{\text{B}}^{\tau\tau}$	$A_{\text{FB}}^{\tau\tau}$ (Counting)	$A_{\text{FB}}^{\tau\tau}$ (Fitting)
91.254	3080	2979	0.017 ± 0.013	0.016 ± 0.012
88.480	66	100	-0.205 ± 0.076	-0.252 ± 0.068
89.472	128	161	-0.114 ± 0.058	-0.099 ± 0.054
90.227	268	301	-0.058 ± 0.042	-0.070 ± 0.039
91.224	1817	1786	0.009 ± 0.017	0.001 ± 0.016
91.969	377	357	0.027 ± 0.037	0.040 ± 0.035
92.968	239	197	0.096 ± 0.048	0.096 ± 0.044
93.717	206	153	0.148 ± 0.052	0.171 ± 0.048

Table 10: The 1991 forward-backward asymmetry for $e^+e^- \rightarrow \tau^+\tau^-$ within $|\cos\theta| < 0.90$ and the acollinearity angle less than 15° , from a total of 12215 events. The systematic error of the measurements is 0.003. The forward-backward asymmetries in column four were obtained from the numbers in columns two and three; column five represents the results from a maximum likelihood fit to the $\cos\theta$ distribution.

	Without Lepton Universality	With Lepton Universality
$C_{ZZ}^s(e^+e^-) \equiv \kappa_{ZZ}^s(\hat{g}_a^{e^2} + \hat{g}_v^{e^2})(\hat{g}_a^{e^2} + \hat{g}_v^{e^2})$	0.0624±0.0010	
$C_{ZZ}^s(\mu^+\mu^-) \equiv \kappa_{ZZ}^s(\hat{g}_a^{e^2} + \hat{g}_v^{e^2})(\hat{g}_a^{\mu^2} + \hat{g}_v^{\mu^2})$	0.06350±0.00085	
$C_{ZZ}^s(\tau^+\tau^-) \equiv \kappa_{ZZ}^s(\hat{g}_a^{e^2} + \hat{g}_v^{e^2})(\hat{g}_a^{\tau^2} + \hat{g}_v^{\tau^2})$	0.06194±0.00098	
$C_{ZZ}^s(\ell^+\ell^-) \equiv \kappa_{ZZ}^s(\hat{g}_a^{\ell^2} + \hat{g}_v^{\ell^2})^2$		0.06280±0.00075
$C_{ZZ}^a(e^+e^-) \equiv \kappa_{ZZ}^a \hat{g}_a^e \hat{g}_v^e \hat{g}_a^e \hat{g}_v^e$	-0.00005±0.00024	
$C_{ZZ}^a(\mu^+\mu^-) \equiv \kappa_{ZZ}^a \hat{g}_a^e \hat{g}_v^e \hat{g}_a^\mu \hat{g}_v^\mu$	0.00010±0.00016	
$C_{ZZ}^a(\tau^+\tau^-) \equiv \kappa_{ZZ}^a \hat{g}_a^e \hat{g}_v^e \hat{g}_a^\tau \hat{g}_v^\tau$	0.00034±0.00017	
$C_{ZZ}^a(\ell^+\ell^-) \equiv \kappa_{ZZ}^a(\hat{g}_a^\ell \hat{g}_v^\ell)^2$		0.00016±0.00011
$C_{\gamma Z}^a(e^+e^-) \equiv \kappa_{\gamma Z}^a \hat{g}_a^e \hat{g}_a^e$	0.183±0.051	
$C_{\gamma Z}^a(\mu^+\mu^-) \equiv \kappa_{\gamma Z}^a \hat{g}_a^e \hat{g}_a^\mu$	0.208±0.027	
$C_{\gamma Z}^a(\tau^+\tau^-) \equiv \kappa_{\gamma Z}^a \hat{g}_a^e \hat{g}_a^\tau$	0.225±0.028	
$C_{\gamma Z}^a(\ell^+\ell^-) \equiv \kappa_{\gamma Z}^a \hat{g}_a^{\ell^2}$		0.215±0.018
$C_{\gamma Z}^s(e^+e^-) \equiv \kappa_{\gamma Z}^s \hat{g}_v^e \hat{g}_v^e$	-0.023±0.034	
$C_{\gamma Z}^s(\mu^+\mu^-) \equiv \kappa_{\gamma Z}^s \hat{g}_v^e \hat{g}_v^\mu$	0.018±0.022	
$C_{\gamma Z}^s(\tau^+\tau^-) \equiv \kappa_{\gamma Z}^s \hat{g}_v^e \hat{g}_v^\tau$	0.027±0.024	
$C_{\gamma Z}^s(\ell^+\ell^-) \equiv \kappa_{\gamma Z}^s \hat{g}_v^{\ell^2}$		0.013±0.015
M_Z [GeV]	91.181±0.007±0.006	91.181±0.007±0.006
Γ_Z [GeV]	2.483±0.011±0.004	2.483±0.011±0.004
$\sigma_{\text{had}}^{\text{pole}}$ [nb]	41.45±0.31	41.45±0.31
χ^2/NDOF	55.8/90	64.6/98

Table 11: Results of the model-independent fits to the leptonic cross sections and forward-backward asymmetries. The hadronic cross section measurements are also included in both fits. The values obtained for χ^2 in the parameter fits are dominated by the size of the statistical errors. When the fits were repeated with the values of systematic errors set to zero, the resulting χ^2 values were 57.0 and 66.6 for the fits in columns 2 and 3, respectively.

Determination Related to	Parameters Used	$\hat{g}_a^{\ell^2}$	$\hat{g}_v^{\ell^2}$
Z-exchange only	$C_{ZZ}^s \equiv (\hat{g}_a^{\ell^2} + \hat{g}_v^{\ell^2})^2$ $C_{ZZ}^a \equiv \hat{g}_a^{\ell^2} \hat{g}_v^{\ell^2}$	0.2500 ± 0.0017	0.00064 ± 0.00044
γ Z-interference only	$C_{\gamma Z}^a \equiv \hat{g}_a^{\ell^2}$ $C_{\gamma Z}^s \equiv \hat{g}_v^{\ell^2}$	0.215 ± 0.018	0.013 ± 0.015
cross sections only	$C_{ZZ}^s \equiv (\hat{g}_a^{\ell^2} + \hat{g}_v^{\ell^2})^2$ $C_{\gamma Z}^s \equiv \hat{g}_v^{\ell^2}$	0.238 ± 0.015	0.013 ± 0.015
$\cos \theta$ terms only	$C_{ZZ}^a \equiv \hat{g}_a^{\ell^2} \hat{g}_v^{\ell^2}$ $C_{\gamma Z}^a \equiv \hat{g}_a^{\ell^2}$	0.215 ± 0.018	0.00074 ± 0.00051
combined result		0.2498 ± 0.0016	0.00071 ± 0.00044

Table 12: Effective leptonic couplings, $\hat{g}_a^{\ell^2}$ and $\hat{g}_v^{\ell^2}$, derived from various combinations of values obtained for the C parameters from the model-independent fit (Table 11, column 3) with lepton universality imposed and κ parameters set equal to 1.

Without Lepton Universality:	
Γ_{ee}	83.03 ± 0.66
$\Gamma_{\mu\mu}$	84.43 ± 0.92
$\Gamma_{\tau\tau}$	82.2 ± 1.1
Γ_{had}	1743 ± 15
With Lepton Universality:	
$\Gamma_{\ell\ell}$	83.27 ± 0.50
Γ_{had}	1738 ± 12

Table 13: Z^0 partial decay widths [MeV] obtained by parameter transformation from $\sigma_{\text{had}}^{\text{pole}}$ and the C_{ZZ}^s parameters in table 11.

	Without Lepton Universality	With Lepton Universality	SM Pre- diction
R_e	20.99 ± 0.25		
R_μ	20.65 ± 0.17		
R_τ	21.22 ± 0.25		
R_ℓ		20.88 ± 0.13	$20.75^{+0.02}_{-0.03}$
$A_{\text{FB}}^{\text{pole}}(e^+e^-)$	-0.002 ± 0.012		
$A_{\text{FB}}^{\text{pole}}(\mu^+\mu^-)$	0.0047 ± 0.0076		
$A_{\text{FB}}^{\text{pole}}(\tau^+\tau^-)$	0.0165 ± 0.0082		
$A_{\text{FB}}^{\text{pole}}$		0.0076 ± 0.0050	$0.014^{+0.006}_{-0.003}$
M_Z [GeV]	$91.181 \pm 0.007 \pm 0.006$	$91.181 \pm 0.007 \pm 0.006$	input
Γ_Z [GeV]	$2.483 \pm 0.011 \pm 0.004$	$2.483 \pm 0.011 \pm 0.004$	$2.489^{+0.022}_{-0.018}$
$\sigma_{\text{had}}^{\text{pole}}$ [nb]	41.45 ± 0.31	41.45 ± 0.31	$41.46^{+0.06}_{-0.03}$

Table 14: Results from a parameter transformation of our model independent analysis into the standard LEP parameter set. The second error quoted on M_Z and Γ_Z is due to the uncertainty of the LEP energy. In the last column we give the Standard Model value for each parameter assuming $M_t = 150$ GeV, $M_H = 300$ GeV and $\alpha_s(M_Z^2) = 0.12$, fixed. The range quoted for the Standard Model prediction reflects variations of M_t in the interval $50 < M_t$ (GeV) < 230 and M_H in the interval $60 < M_H$ (GeV) < 1000 .

A Appendix: Correlation Matrices

Parameter	1	2	3	4	5	6	7
1 M_Z	1.000	.020	-.040	-.002	-.002	.018	-.076
2 $\sigma_{\text{had}}^{\text{pole}}$.020	1.000	.418	-.143	.026	.017	-.023
3 C_{ZZ}^s	-.040	.418	1.000	.691	.062	.022	.058
4 Γ_Z	-.002	-.143	.691	1.000	.047	.009	.021
5 $C_{\gamma Z}^a$	-.002	.026	.062	.047	1.000	.047	-.029
6 C_{ZZ}^a	.018	.017	.022	.009	.047	1.000	.012
7 $C_{\gamma Z}^s$	-.076	-.023	.058	.021	-.029	.012	1.000

Table 15: The parameter correlation matrix for the extended effective Born approach assuming lepton universality. The results of this fit are summarized in Table 11 column 3.

Parameter	1	2	3	4	5	6	7	8	9	10	11	12	13	14	15
1 M_Z	1.000	.017	-.074	-.017	-.020	.007	-.009	.064	.010	-.036	.090	.029	-.079	-.073	-.094
2 $\sigma_{\text{had}}^{\text{pole}}$.017	1.000	.373	.390	.327	-.121	-.036	.045	.045	.077	.010	.022	-.071	.000	.008
3 $C_{ZZ}^s(e^+e^-)$	-.074	.373	1.000	.582	.488	.525	-.046	.054	.057	.136	.003	.030	-.003	.030	.056
4 $C_{ZZ}^s(\mu^+\mu^-)$	-.017	.390	.582	1.000	.544	.631	-.017	.096	.064	.042	.034	.040	-.053	.128	.045
5 $C_{ZZ}^s(\tau^+\tau^-)$	-.020	.327	.488	.544	1.000	.549	-.013	.054	.110	.033	.015	.065	-.041	.020	.159
6 Γ_Z	.007	-.121	.525	.631	.549	1.000	.004	.061	.061	-.005	.023	.043	-.024	.025	.051
7 $C_{\gamma Z}^a(e^+e^-)$	-.009	-.036	-.046	-.017	-.013	.004	1.000	-.002	-.002	.007	.000	.000	.184	.000	-.001
8 $C_{\gamma Z}^a(\mu^+\mu^-)$.064	.045	.054	.096	.054	.061	-.002	1.000	.007	.002	.213	.006	-.012	-.071	-.003
9 $C_{\gamma Z}^a(\tau^+\tau^-)$.010	.045	.057	.064	.110	.061	-.002	.007	1.000	.003	.003	.180	-.007	.000	-.120
10 $C_{ZZ}^a(e^+e^-)$	-.036	.077	.136	.042	.033	-.005	.007	.002	.003	1.000	-.009	-.005	-.012	.010	.012
11 $C_{ZZ}^a(\mu^+\mu^-)$.090	.010	.003	.034	.015	.023	.000	.213	.003	-.009	1.000	.009	-.011	.061	-.011
12 $C_{ZZ}^a(\tau^+\tau^-)$.029	.022	.030	.040	.065	.043	.000	.006	.180	-.005	.009	1.000	-.008	-.005	.035
13 $C_{\gamma Z}^s(e^+e^-)$	-.079	-.071	-.003	-.053	-.041	-.024	.184	-.012	-.007	-.012	-.011	-.008	1.000	.024	.023
14 $C_{\gamma Z}^s(\mu^+\mu^-)$	-.073	.000	.030	.128	.020	.025	.000	-.071	.000	.010	.061	-.005	.024	1.000	.033
15 $C_{\gamma Z}^s(\tau^+\tau^-)$	-.094	.008	.056	.045	.159	.051	-.001	-.003	-.120	.012	-.011	.035	.023	.033	1.000

Table 16: The parameter correlation matrix for the extended effective Born approach without assuming lepton universality. The results of this fit are summarized in Table 11 column 2.

Parameter	1	2	3	4	5
1 M_Z	1.000	.018	.024	.000	.020
2 $\sigma_{\text{had}}^{\text{pole}}$.018	1.000	.193	-.144	.009
3 R_ℓ	.024	.193	1.000	.080	-.001
4 Γ_Z	.000	-.144	.080	1.000	-.005
5 $A_{\text{FB}}^{\text{pole}}$.020	.009	-.001	-.005	1.000

Table 17: The parameter correlation matrix for the standard LEP parametrization assuming lepton universality. The results of this fit are summarized in Table 14 column 3.

Parameter	1	2	3	4	5	6	7	8	9
1 M_Z	1.000	.010	.076	-.008	-.008	.008	-.036	.083	.032
2 $\sigma_{\text{had}}^{\text{pole}}$.010	1.000	.026	.135	.103	-.131	.078	-.004	.003
3 R_e	.076	.026	1.000	.096	.041	.030	-.144	.019	.008
4 R_μ	-.008	.135	.096	1.000	.038	.044	.000	.004	.000
5 R_τ	-.008	.103	.041	.038	1.000	.020	.004	-.001	.004
6 Γ_Z	.008	-.131	.030	.044	.020	1.000	-.005	.003	.012
7 $A_{\text{FB}}^{\text{pole}}(e^+e^-)$	-.036	.078	-.144	.000	.004	-.005	1.000	-.011	-.007
8 $A_{\text{FB}}^{\text{pole}}(\mu^+\mu^-)$.083	-.004	.019	.004	-.001	.003	-.011	1.000	.009
9 $A_{\text{FB}}^{\text{pole}}(\tau^+\tau^-)$.032	.003	.008	.000	.004	.012	-.007	.009	1.000

Table 18: The parameter correlation matrix for the standard LEP parametrization without assuming lepton universality. The results of this fit are summarized in Table 14 column 2.

Parameter	1	2
1 M_Z	6^2	-3^2
2 Γ_Z	-3^2	4^2

Table 19: Covariance matrix elements originating from uncertainties in the centre-of-mass energy, in MeV^2 . These uncertainties were evaluated by comparisons of fits performed with and without uncertainties in the energy scale taken into account and are common to all LEP experiments. In the parameter errors quoted, and the correlation matrices in Table 15–18, the effects of the LEP centre-of-mass energy uncertainty have already been included. They have been separated here to facilitate the combination of results from different experiments.

References

- [1] OPAL Collaboration, G. Alexander et al., *Z. Phys.* **C52** (1991) 175.
- [2] L. Arnaudon et al., CERN-PPE/92-125 and CERN-SL/92-37(DI).
- [3] OPAL Collaboration, K. Ahmet et al., *Nucl. Inst. Meth.* **A305** (1991) 275.
- [4] T. Sjöstrand, *Comp. Phys. Comm.* **39** (1986) 347; JETSET, Version 7.2.
- [5] G. Marchesini and B.R. Webber, *Nucl. Phys.* **B310** (1988) 461.
- [6] OPAL Collaboration, M.Z. Akrawy et al., *Z. Phys.* **C47** (1990) 505.
- [7] S. Jadach et al., *Comp. Phys. Comm.* **66** (1991) 276.
- [8] M. Böhm, A. Denner and W. Hollik, *Nucl. Phys.* **B304** (1988) 687;
F. A. Berends, R. Kleiss, W. Hollik, *Nucl. Phys.* **B304** (1988), 712.
- [9] S. Jadach et al., *Comp. Phys. Comm.* **70** (1992) 305.
- [10] J. Allison et al., *Nucl. Inst. Meth.* **A317** (1992) 47.
- [11] B.E. Anderson et al., *Nucl. Inst. Meth.*, **A283** (1989) 650;
D.C. Imrie et al. *Nucl. Inst. Meth.* **A283** (1989) 515.
- [12] M. Arignon et al., *Nucl. Inst. Meth.* **A313** (1992) 103.
- [13] F.A. Berends and R. Kleiss, *Nucl. Phys.* **B186** (1981) 22.
- [14] S. Jadach, Private Communication.
- [15] M. Caffo, H. Czyz and E. Remiddi, *Il Nuovo Cimento* **105 A** (1992) 277.
- [16] W. Beenakker and B. Pietrzyk, *Phys. Lett.* **B296** (1992) 244.
- [17] D. Charlton et al., CERN-PPE/92-136 (1992).
- [18] Line shape program ZFITTER, version 451, including an implementation of $e^+e^- \rightarrow 4$ fermions.
Dubna-Zeuthen radiative correction group, D. Bardin et al.
D. Bardin et al., *Comp. Phys. Comm.* **59** (1990) 303; *Z. Phys.* **C44** (1989) 493; *Nucl. Phys.* **B351**
(1991) 1; *Phys. Lett.* **B229** (1989) 405; CERN-TH 6443/92 (May 1992).
- [19] W. Beenakker et al., *Nucl. Phys.* **B349** (1991) 323.
- [20] M. Consoli and W. Hollik, *Z Physics at LEP1*, CERN 89-08, ed. G. Altarelli et al., Vol 1 (1989) 7.
- [21] A. Borrelli et al., *Nucl. Phys.* **B333** (1990) 357;
R. Stuart, *Phys. Lett.* **B262** (1991) 113; *Phys. Lett.* **B272** (1991) 353; prepr. CERN-TH.6261/91
(1991);
A. Leike, T. Riemann and J. Rose, *Phys. Lett.* **B273** (1991) 513.
- [22] K.G. Chetyrkin and J.H. Kühn, *Phys. Lett.* **B248** (1990) 359.
- [23] CDF Collaboration, F. Abe et al., *Phys. Rev. Lett.* **65** (1990) 2243; *Phys. Rev.* **D43** (1991) 2070;
UA2 Collaboration, J. Alitti et al., *Phys. Lett.* **B276** (1992) 354.
- [24] OPAL Collaboration, P. Acton et al., *Z. Phys.* **C55** (1992) 1.

- [25] ALEPH Collaboration, D. Decamp et al., Z. Phys. **C53** (1992) 1;
 DELPHI Collaboration, P. Abreu et al., Nucl. Phys. **B367** (1991) 511;
 L3 Collaboration, B. Adeva et al., Z. Phys. **C51** (1991) 179;
 The LEP Collaborations: ALEPH, DELPHI, L3 and OPAL, Phys. Lett. **B276** (1992) 247.

Figure Captions

Figure 1: A schematic diagram of the elements of the 1992 OPAL forward detectors used in the 1991 luminosity determination. The calorimeter consists of a presampler section of 4 radiation lengths and a main section of 19 radiation lengths. The set of drift chambers nearest the interaction region was installed for 1992 data taking. The sense wires of these drift chambers are located close to the inner edge of the acceptance for luminosity events.

Figure 2: A comparison of the performance of the forward detector tube chambers in 1991 and 1992. For both sets of data, luminosity events were selected at the inner edge of the acceptance of the left hand forward detector: $|\theta_L - 0.065| < 2$ mrad. For these events the plots show, for 1991 and 1992, the radius measured by the right hand forward detector, R_R , minus the radius measured by the left hand forward detector, R_L , as a function of ϕ_L . The structure observed in both plots arises from inhomogeneity of the tube chambers and variations in gain. These local distortions are consistent between the two years with a $\chi^2 = 45.8$ for 44 degrees of freedom. If there had been significant changes in the performance of the tubes between the years then one would have expected the structure in the plots also to have changed.

Figure 3: The total energy in the forward detector versus the total energy in the electromagnetic calorimeter for the data (a) and the Monte Carlo (b) after all the selection cuts for hadrons except for the R_{vis} cut. The selection cut of $R_{vis} > 0.09$ is shown as a line in the plot. The distributions of R_{vis} for the data (points) and Monte Carlo (histogram) are shown in (c). The open and shaded histograms are the Monte Carlo distributions for the sum of the processes $e^+e^- \rightarrow \text{hadrons}$ and $e^+e^- \rightarrow \tau^+\tau^-$ and for $\tau^+\tau^-$ events only, respectively.

Figure 4: The lower part of the invariant mass distributions after all the selection cuts for hadrons except for the invariant mass cut. The open and shaded histograms are the Monte Carlo distributions for the sum of the processes $e^+e^- \rightarrow \text{hadrons}$ and $e^+e^- \rightarrow \tau^+\tau^-$ and for $\tau^+\tau^-$ events only, respectively.

Figure 5: Comparison of the parameters from the model independent fit (Table 11 column 3) with the Standard Model prediction as a function of M_t . The cross-hatched area shows the variation of the Standard Model prediction with M_H spanning the interval $60 < M_H (\text{GeV}) < 1000$ and the singly-hatched area corresponds to a variation of $\alpha_s(M_Z^2)$ within the interval $0.11 < \alpha_s(M_Z^2) < 0.13$. The experimental errors on the parameters are indicated as vertical bands.

Figure 6: One standard deviation contours (39% probability content) in the $R_\ell - A_{\text{FB}}^{\text{pole}}$ plane for each leptonic species and for all leptons assuming lepton universality. The shaded area is the Standard Model prediction for $50 < M_t (\text{GeV}) < 230$ and $60 < M_H (\text{GeV}) < 1000$.

Figure 7: Cross sections as functions of centre-of-mass energy for:

- a) $e^+e^- \rightarrow \text{hadrons}$, corrected for acceptance;
- b) $e^+e^- \rightarrow e^+e^-$, integrated over $|\cos\theta| < 0.7$ and corrected for efficiency within the geometrical acceptance;
- c) $e^+e^- \rightarrow \mu^+\mu^-$, corrected for acceptance;
- d) $e^+e^- \rightarrow \tau^+\tau^-$, corrected for acceptance.

The solid lines are the results of the fit to the combined e^+e^- , $\mu^+\mu^-$, $\tau^+\tau^-$ and hadronic data described in the text. The solid points show the 1991 data and the open points the 1990 data. Only statistical errors are shown. The lower plots display the residuals to the Standard Model fit.

Figure 8: Forward-backward asymmetries for:

- a) $e^+e^- \rightarrow e^+e^-$, within $|\cos\theta| < 0.7$;
- b) $e^+e^- \rightarrow \mu^+\mu^-$, within $|\cos\theta| < 0.95$;
- c) $e^+e^- \rightarrow \tau^+\tau^-$, within $|\cos\theta| < 0.90$.
- d) The difference averaged over all 3 leptonic species between the measured forward-backward asymmetry and the Standard Model fit result.

The solid lines are the results of the fit to the combined e^+e^- , $\mu^+\mu^-$, $\tau^+\tau^-$ and hadronic data described in the text. The solid points show the 1991 data and the open points the 1990 data. Only statistical errors are shown.

Figure 9: The χ^2 curves for the fit to M_t and $\alpha_s(M_Z^2)$, using the OPAL cross section and forward-backward asymmetry measurements, for three different Higgs mass values spanning the interval $60 < M_H(\text{GeV}) < 1000$. The minimum value of χ^2 from the $M_H = 1000$ GeV curve has been subtracted from all curves. In these fits the strong coupling constant is unconstrained. The solid lines refer to a direct fit to cross sections and leptonic asymmetries, the dashed line refers to a fit to the set of 7 parameters (Table 11 column 3) from our model independent fit.

OPAL Forward Detector

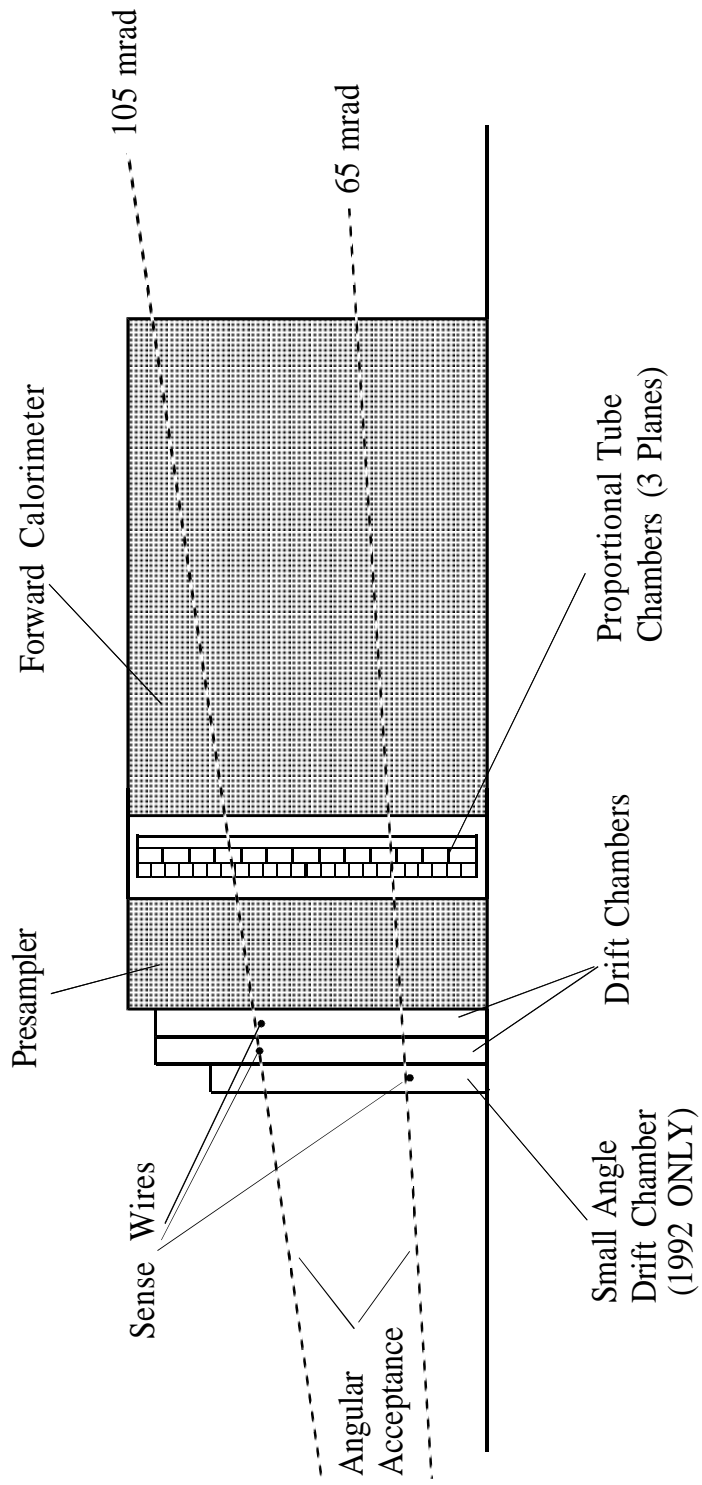


Figure 1:

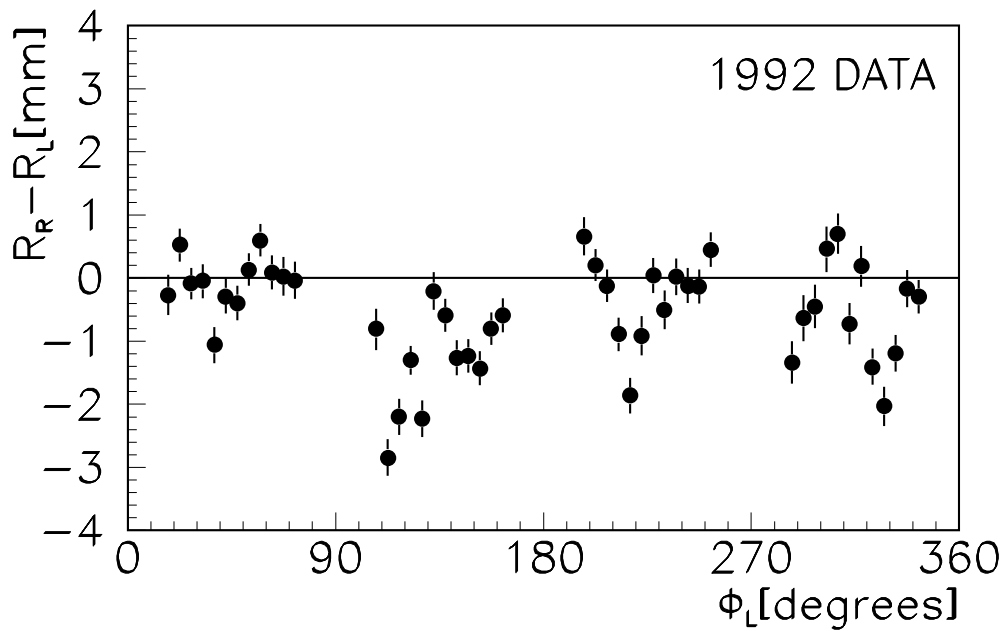
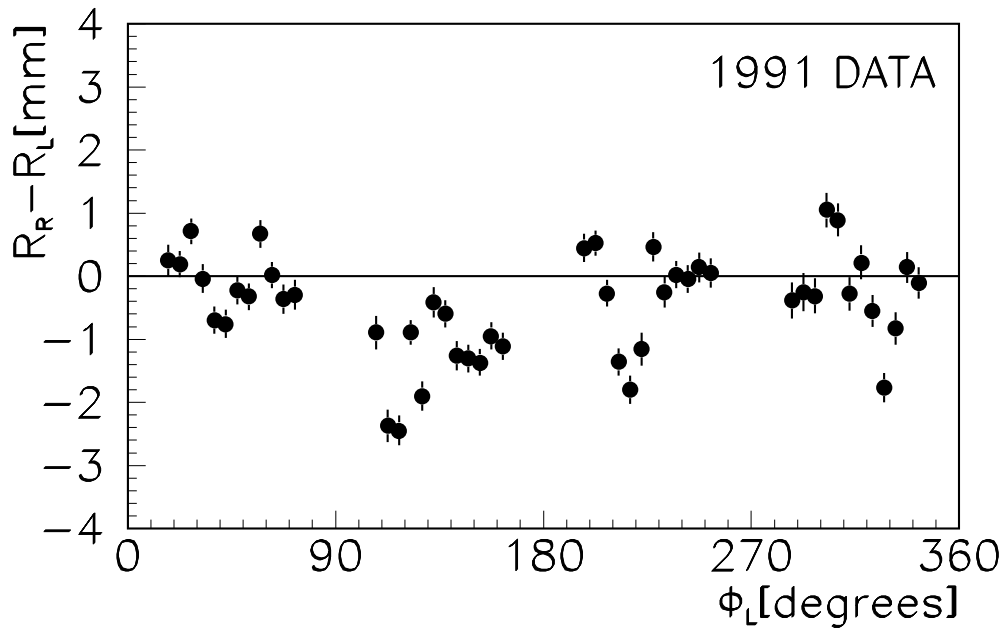


Figure 2:

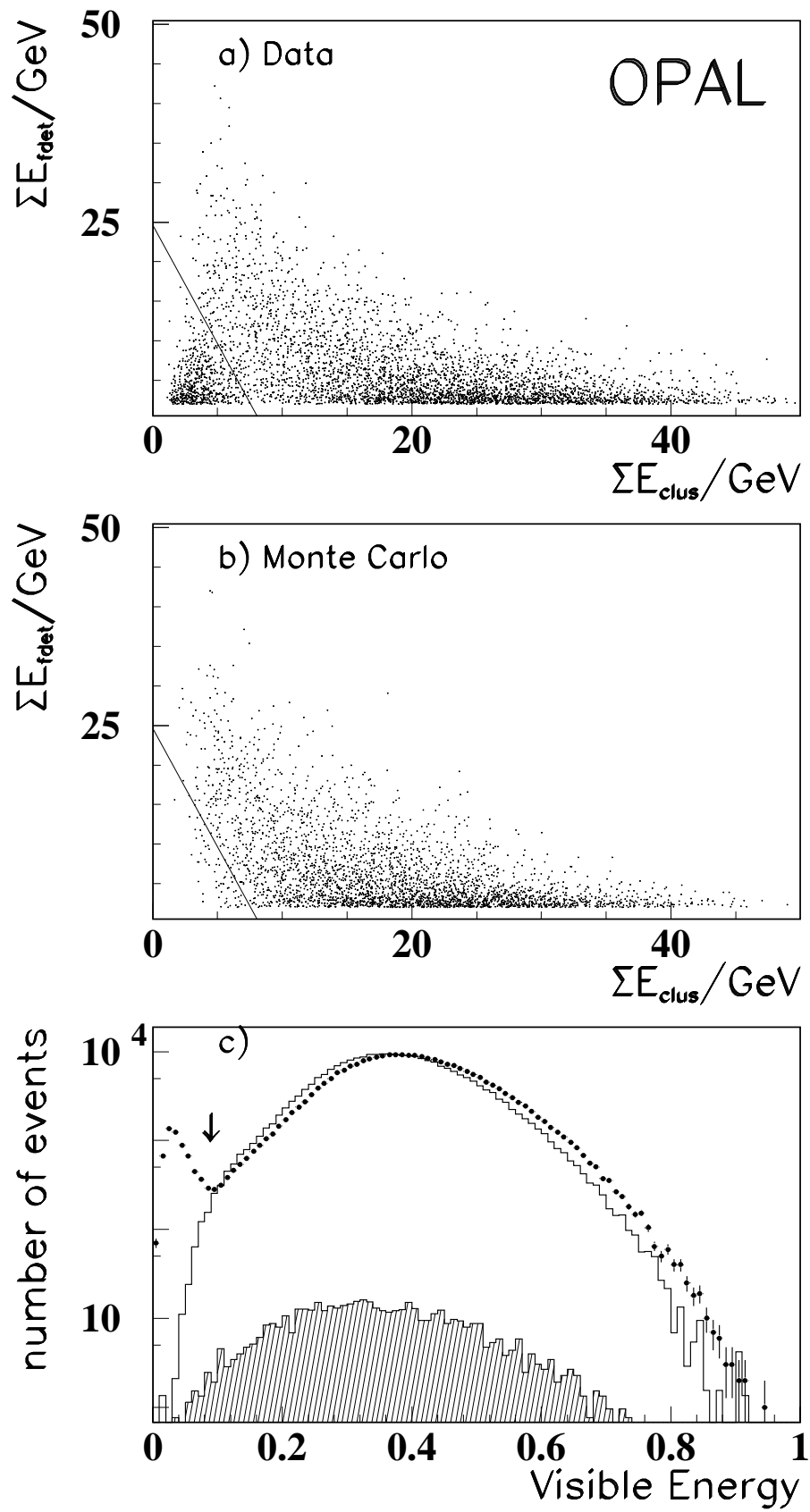


Figure 3:

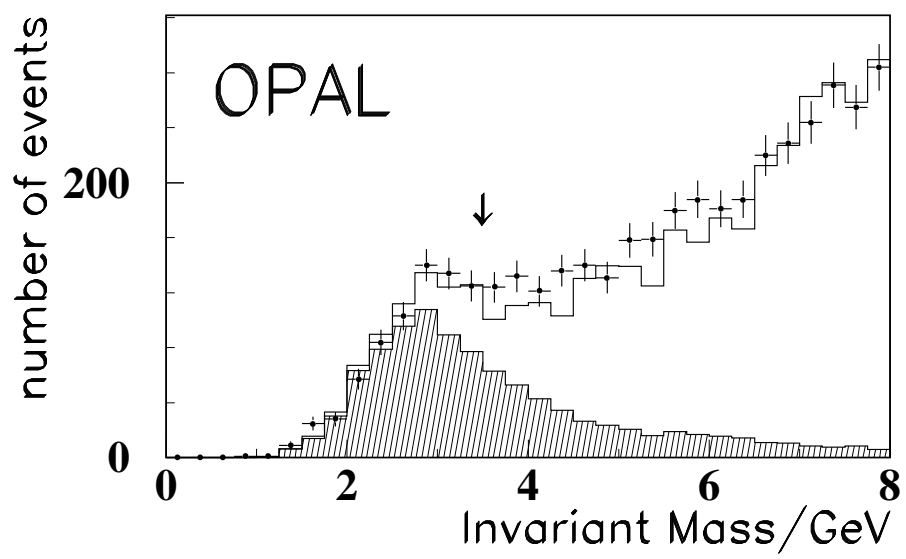


Figure 4:

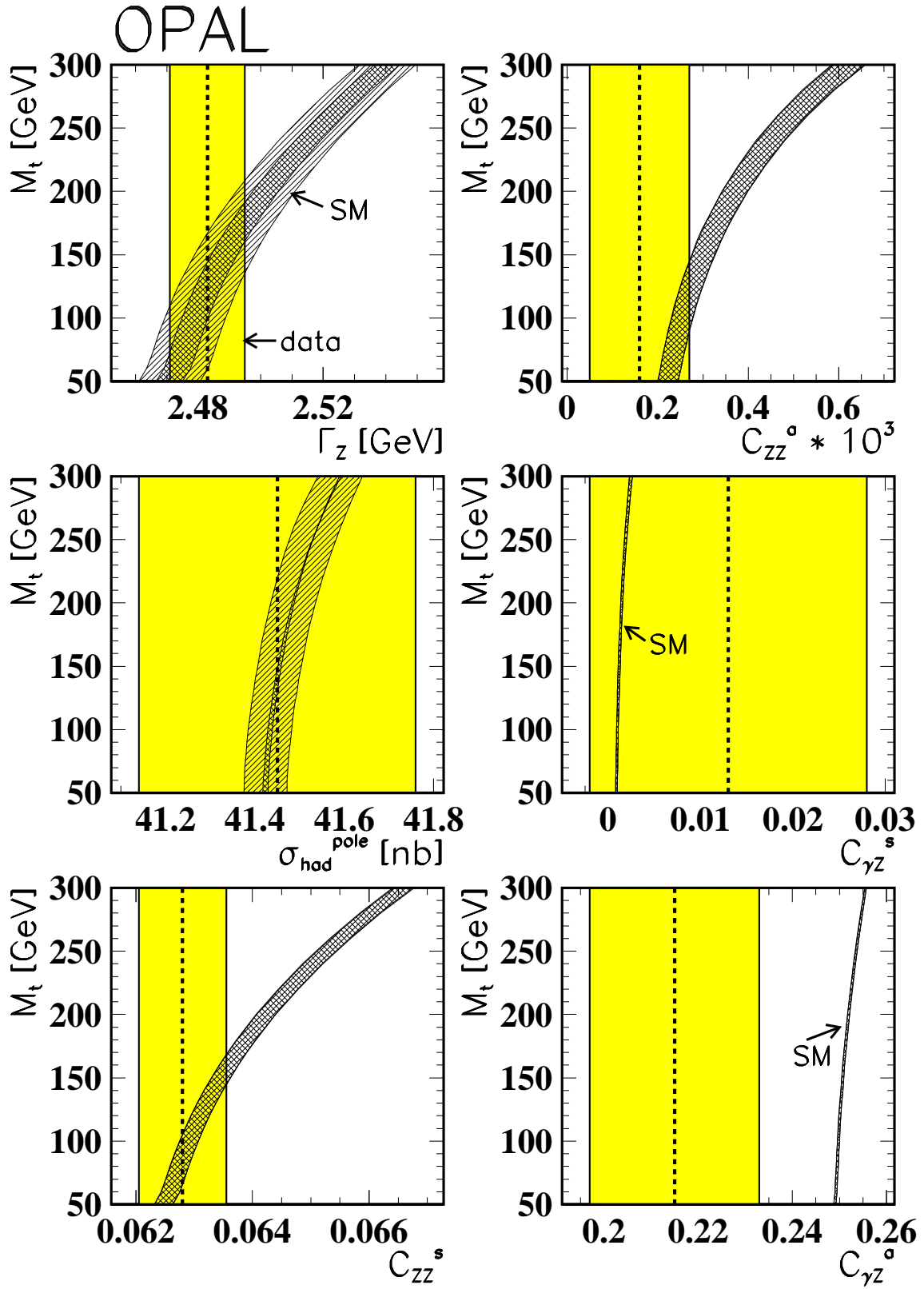


Figure 5:

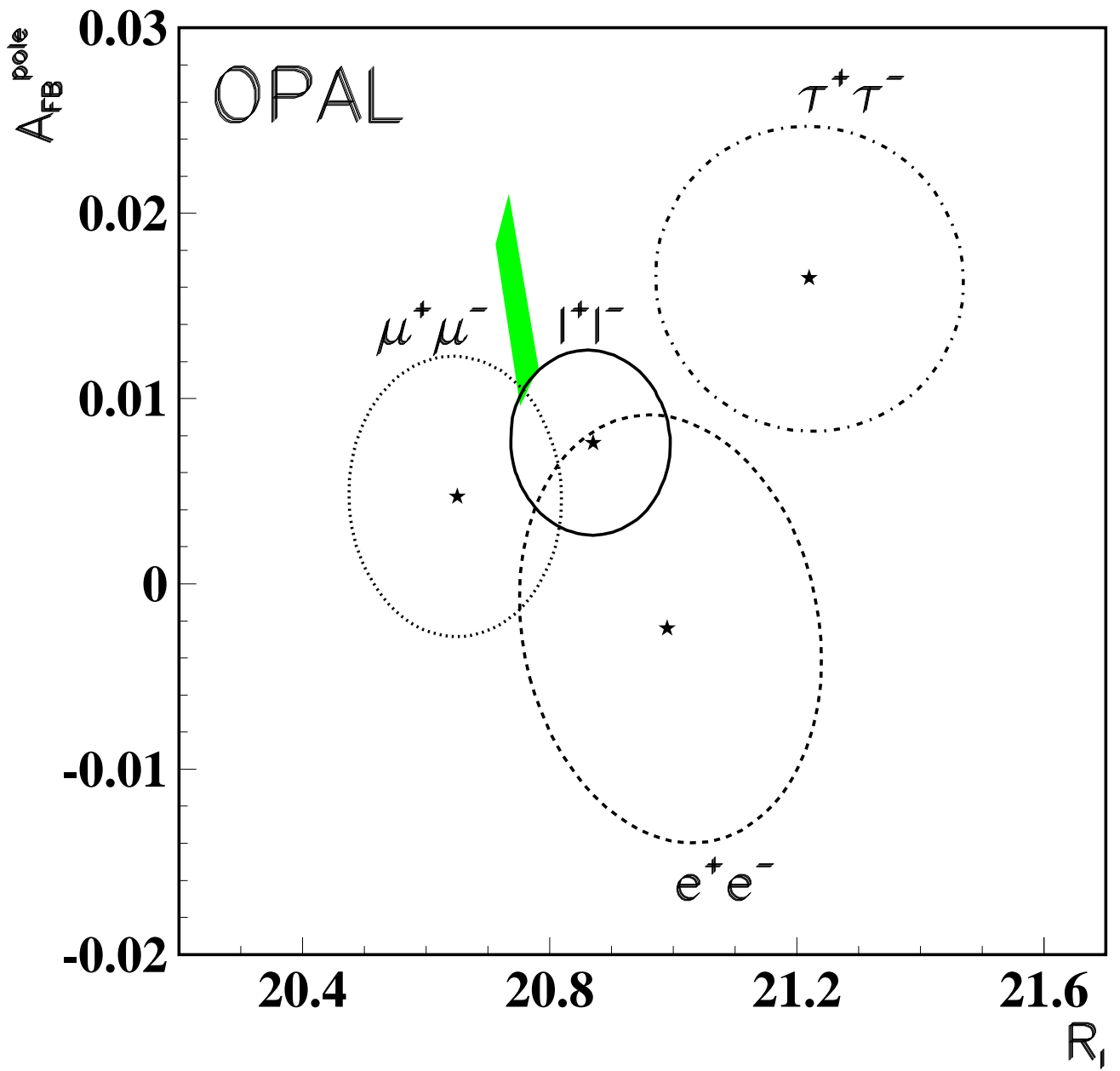


Figure 6:

OPAL

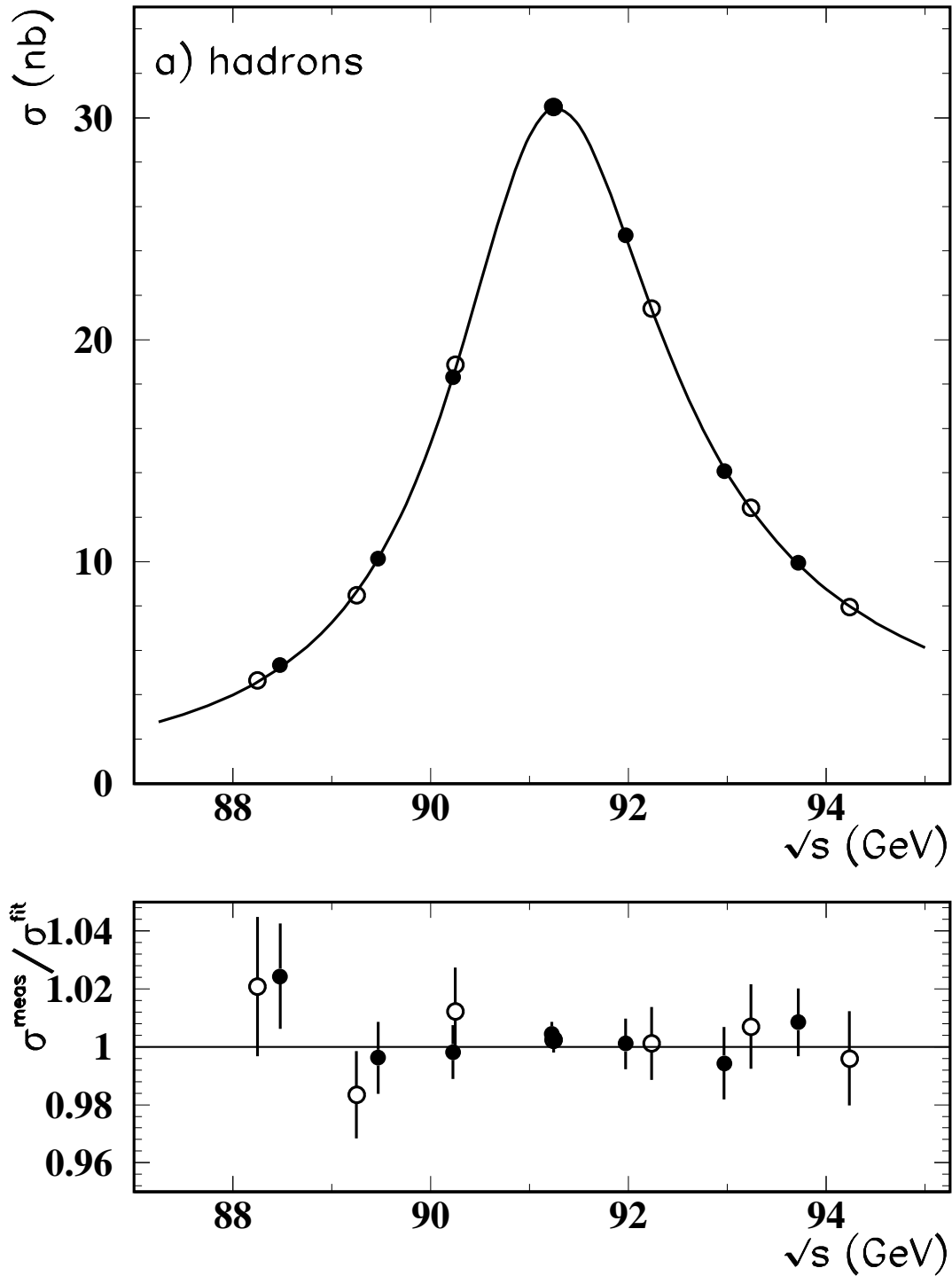


Figure 7:

OPAL

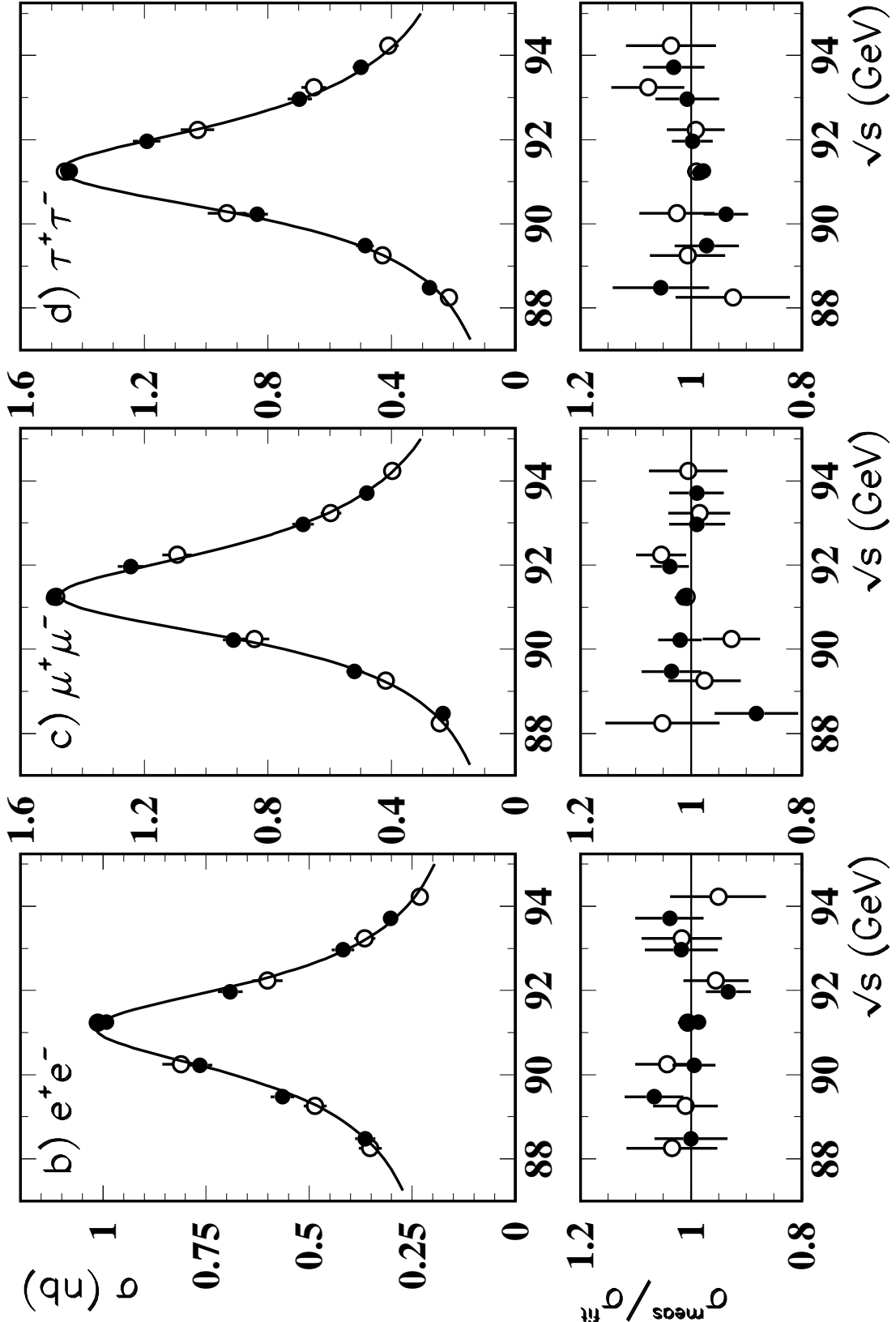


Figure 7:

OPAL

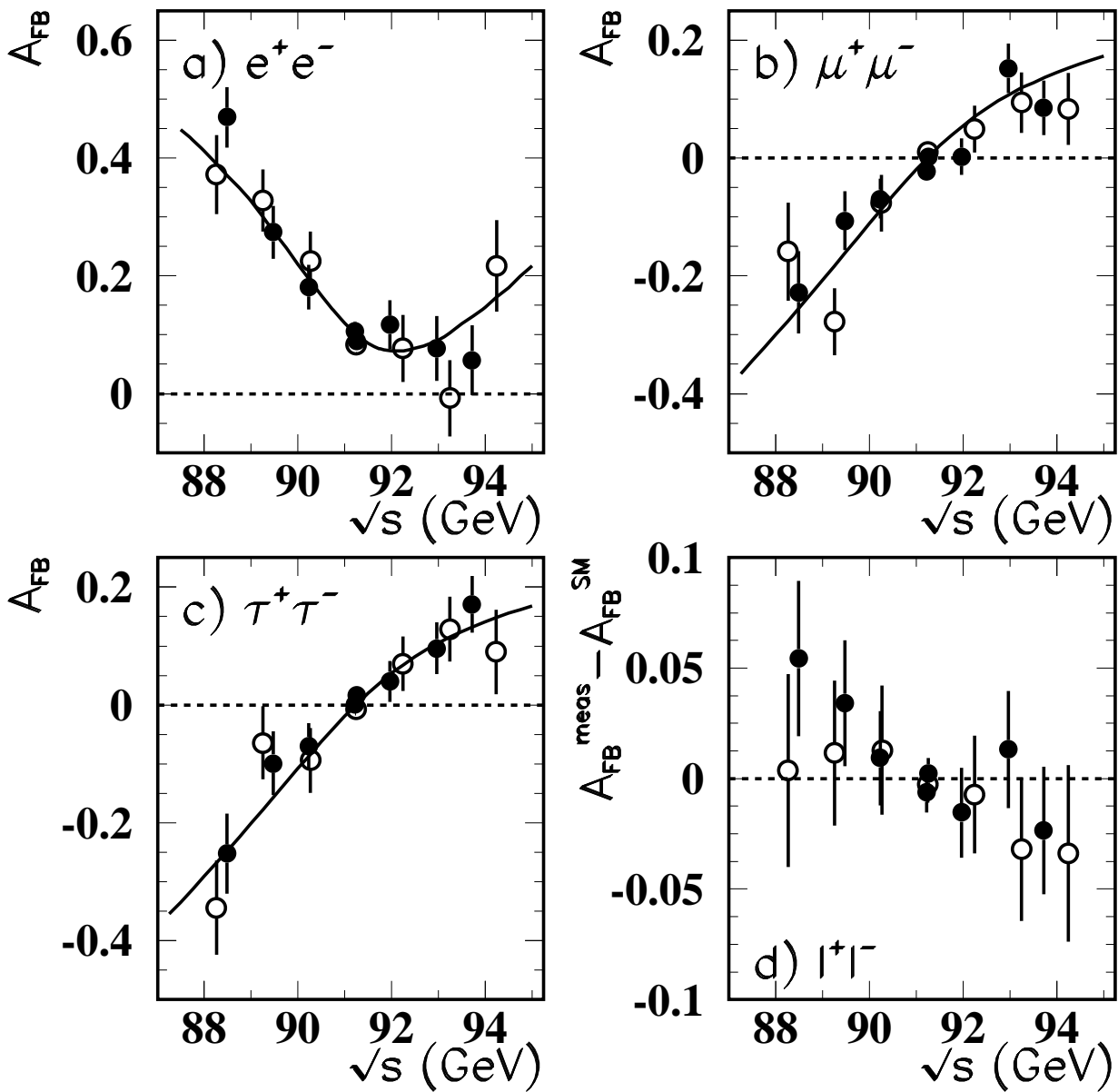


Figure 8:

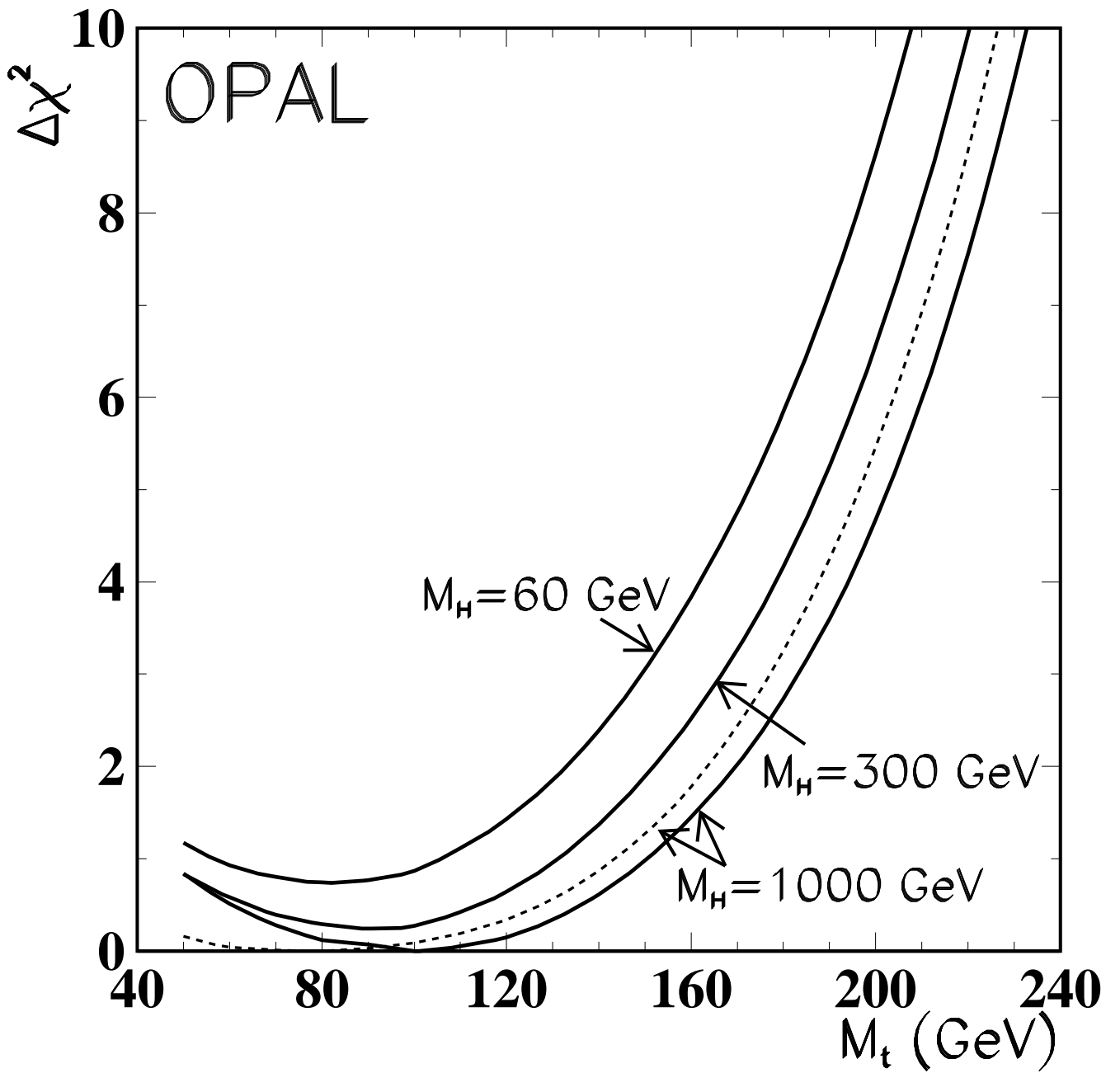


Figure 9: